



UNIVERSITY OF LEEDS

This is a repository copy of *Coupled RANS-LPT modelling of dilute, particle-laden flow in a duct with a 90° bend*.

White Rose Research Online URL for this paper:  
<http://eprints.whiterose.ac.uk/79572/>

Version: Accepted Version

---

**Article:**

Njobuenwu, DO, Fairweather, M and Yao, J (2013) Coupled RANS-LPT modelling of dilute, particle-laden flow in a duct with a 90° bend. *International Journal of Multiphase Flow*, 50. 71 - 88. ISSN 0301-9322

<https://doi.org/10.1016/j.ijmultiphaseflow.2012.10.009>

---

**Reuse**

Unless indicated otherwise, fulltext items are protected by copyright with all rights reserved. The copyright exception in section 29 of the Copyright, Designs and Patents Act 1988 allows the making of a single copy solely for the purpose of non-commercial research or private study within the limits of fair dealing. The publisher or other rights-holder may allow further reproduction and re-use of this version - refer to the White Rose Research Online record for this item. Where records identify the publisher as the copyright holder, users can verify any specific terms of use on the publisher's website.

**Takedown**

If you consider content in White Rose Research Online to be in breach of UK law, please notify us by emailing [eprints@whiterose.ac.uk](mailto:eprints@whiterose.ac.uk) including the URL of the record and the reason for the withdrawal request.



[eprints@whiterose.ac.uk](mailto:eprints@whiterose.ac.uk)  
<https://eprints.whiterose.ac.uk/>

# **Coupled RANS-LPT Modelling of Dilute, Particle-Laden Flow in a Duct with a 90° Bend**

**D.O. Njobuenwu<sup>†</sup>, M. Fairweather and J. Yao**

Institute of Particle Science and Engineering, School of Process, Environmental and Materials Engineering, University of Leeds, Leeds LS2 9JT, UK

---

<sup>†</sup>To whom correspondence should be addressed:

Dr. D.O. Njobuenwu, School of Process, Environmental and Materials Engineering,  
University of Leeds, Leeds LS2 9JT, UK

Tel: +44 (0) 113 343 2351; Fax: +44 (0) 113 343 2405;

Email: [d.o.njobuenwu@leeds.ac.uk](mailto:d.o.njobuenwu@leeds.ac.uk)

**Abstract**

A dilute, particle-laden flow in a square duct with a 90° bend is modelled using a RANS approach, coupled to a second-moment turbulence closure, together with a Lagrangian particle tracking technique, with particle dispersion modelled using a stochastic approach that ensures turbulence anisotropy. Detailed predictions of mean and fluctuating fluid and particle velocities are validated through comparisons of predictions with experimental measurements made for gas-solid flows in a vertical-to-horizontal flow configuration. Reasonable agreement between predicted first and second moments and data is found for both phases, with the consistent application of anisotropic and three-dimensional modelling approaches resulting in predictions that compare favourably with those of other authors, and which provide fluctuating particle velocities in acceptable agreement with data.

**Keywords:** Particle-laden flow, duct, 90° bend, RANS, second-moment closure, Lagrangian particle tracking

## 1. Introduction

Particle-laden flows have numerous areas of application (Mohanarangam et al, 2008), and the transport of such flows requires detailed understanding to permit their accurate prediction. Two numerical approaches are generally used in modelling such flows, these being the Eulerian-Eulerian and Eulerian-Lagrangian approaches, with the choice between these two reference frameworks in essence being problem-dependent. The former approach treats both phases as interpenetrating and interacting continua, and the coupled governing equations are then solved for each phase giving the time dependent behaviour of the two phases (Mohanarangam et al, 2008; Tu and Fletcher, 1995). This approach is economical and convenient for implementing two- and four-way coupling between the fluid and particle phases. Its drawback is in the complexity associated with accommodating particle phase fluctuations, particle-wall collisions, certain boundary conditions and poly-dispersed particle sizes. The consideration of a particle size distribution, in particular, requires the solution of a set of equations for each size class considered, and hence the computational effort increases with the number of size classes. The Eulerian-Lagrangian approach differs in not considering the particle phase as a whole, but in tracking individual representative particles in the flow, with their trajectory simulated using Newton's second law of motion (Gouesbet and Berlemont, 1999; Mohanarangam et al, 2007). This method performs well in those areas, noted above, that represent drawbacks for the Eulerian-Eulerian approach, but has a significant problem itself associated with having to simulate large numbers of particle trajectories in order to generate statistically meaningful results. A more complete review of both approaches can be found in Crowe et al. (1996). Despite the pros and cons of both methods, the Eulerian-Lagrangian approach remains the most popular model for use in predicting dilute multiphase flows, particularly due to its ability to model the crossing trajectories of particles caused by particles moving on different paths to the carrier fluid (Chen, 1997). With increasing computer power, in terms of memory and computation speed, high performance Eulerian-Lagrangian models have become very useful and versatile tools for studying the dynamics of particle-laden flows precisely because they account for the discrete nature of the individual particles.

In the Eulerian-Lagrangian approach, while the particles transverse the flow domain they interact with their surroundings, and these interactions dictate the particle dynamics inside the particular geometry under consideration. Interactions with the surroundings are incorporated by modelling the external forces acting on the particles, as well as particle-wall and particle-particle interactions. These interactions are further complicated if the flow is bounded by concave and convex walls, as in the present case, which cause changes in the direction of flow. For dilute suspensions, which form the basis of this study, these interactions are largely dominated by inertial effects since particles of different sizes selectively interact with different scales of fluid motion (Grigoriadis and Kassinos, 2009). Inertial effects are caused by the reluctance of particles to follow exactly the fluid streamlines, which largely depends on the characteristic time scales between the two phases. The relative importance of these time scales is usually expressed by the dimensionless Stokes number, defined as the ratio  $St = \tau_p/\tau_f$ , where  $\tau_f$  is the characteristic time scale of the fluid phase

and  $\tau_p$  is the particle response time which describes the time that a particle needs to adjust to a change in the flow velocity. Particles with high Stokes numbers augment the inertial effect, with the influence of wall collisions becoming important when these particles are driven close to solid surfaces, with such collisions often dominating the motion of large particles. Small particles, with  $St \ll 1$ , in the neighbourhood of a boundary layer diffuse towards the wall surface under the influence of turbulent eddies in the flow. Although these eddies dissipate as they approach the wall, the particles continue to travel towards the surface by the free flight mechanism due to their inertia. Thus, in low Stokes number flows, turbulent diffusion dominates wall collisions. However, if small particles by chance collide with a wall, the wall collision effect does not have a considerable influence on the particle motion if they continue to follow the mean fluid flow soon after the collision. When particles collide with a wall, the influence of wall roughness and particle shape also come into play, affecting the particle rebound velocity and the drag force thereby influencing the particle motion. The “virtual wall” model (Tsuji et al, 1987; Sommerfeld, 1992) can be employed to simulate the influence of wall roughness, as well as treating non-spherical particle-wall collisions (Sommerfeld and Huber, 1999), by redirecting the particle momentum randomly each time a particle collides with a wall (Tsuji et al, 1987).

Large particle rotational velocities lead to a spin lift force arising from the deformation of the flow field around a particle that causes a pressure difference across the particle. Since particles can acquire high rotational velocities after wall collisions, this effect can be of importance in the near wall region (Sommerfeld, 2003). Changes in the direction of a flow, as in a bend, generate velocity and pressure gradients with strong shear layers close to the geometry boundaries, with large gradients inducing a slip-shear force on the particles. Hence, lift forces will occur in particulate flows in curved ducts and need to be accommodated in simulating the particle dispersion. Details of the importance of all external forces acting on particles on their dispersion, with respect to particle size and the density ratio between the two phases, can be found elsewhere (Armenio and Fiorotto, 2001).

To solve the particle equation of motion, the instantaneous fluid velocities in all directions at the particle position are required. Hence, the instantaneous velocities seen by the particles and their effect on the particles’ dispersion and distribution need to be quantified. In the Reynolds-averaged Navier-Stokes (RANS) modelling framework, the instantaneous fluid velocities are decomposed into a mean velocity ( $\bar{u}$ ) and a fluctuating component ( $u'$ ). The mean part is then obtained directly from the time-averaged Eulerian solution (deterministic), whereas the fluctuating part must be obtained separately through stochastic modelling.

Reliable experimental data are needed to validate numerical models, with the Kliafas and Holt (1987) data set often used in the validation of predictions of particle-laden two-phase flows in  $90^\circ$  duct bends. Some of the studies that used these data for validation purpose are those of Tu and co-workers (Tu and Fletcher, 1995; Mohanarangam et al., 2007; Mohanarangam et al., 2008; Tian

et al., 2008) who applied the renormalization group (RNG) theory-based  $k-\varepsilon$  and standard  $k-\varepsilon$  models in the commercial CFD code FLUENT in their simulations. The authors used both Eulerian-Eulerian (Tu and Fletcher, 1995; Mohanarangam et al., 2008) and Eulerian-Lagrangian (Tian et al., 2008) approaches, and compared both approaches (Mohanarangam et al., 2007) in terms of their ability to predict such gas-solid flows. Comparison of predicted gas mean velocities and the root-mean-square (rms) of velocity fluctuations in the streamwise direction with the Kliafas and Holt (1987) experimental measurements for  $Re=3.47 \times 10^5$  showed good agreement. The Eulerian-Eulerian approach showed superior agreement with data for the rms of velocity fluctuations of the particle phase, while the Eulerian-Lagrangian method gave more detailed information about the particle behaviour. There were some discrepancies between predictions and data for the rms of velocity fluctuations around the bend region, with the authors observing an under-prediction of the gas turbulence intensity in the boundary layers on both the inner and outer walls of the bend at angles of  $30^\circ$  and  $45^\circ$ . The authors also reported (Mohanarangam et al., 2007) limitations of the traditional Gosman and Ioannides (1981) model for predicting particle dispersion in gas-particle flows in curved ducts, as evidenced by the poor prediction of the fluctuating particle velocities, with most works that implemented this dispersion model showing similar disparities with particle fluctuating velocity data. More specifically, Mohanarangam et al. (2007) reported that the Eulerian-Lagrangian approach with the Gosman and Ioannides (1981) dispersion model could not quantitatively predict the particle velocity fluctuations, whilst the Eulerian-Eulerian approach gave closer agreement with data. Kuan et al. (2007) also could not predict particle velocity fluctuations with any degree of accuracy, while Kuan et al. (2003) reported an under-prediction of these velocities for a gas-solid flow in a bend. Hence, all these authors (Kuan et al., 2003 and 2007; Mohanarangam et al., 2007) did not report any direct comparisons between their predictions of particle velocity fluctuations and experimental data. Niu (2001) also used the RNG  $k-\varepsilon$  turbulence model to predict gas flows in a duct bend, using the Kliafas and Holt (1987) data for  $Re=3.47 \times 10^5$  for validation purposes prior to modelling wall erosion by particles. Fair agreement between predictions and data was obtained for gas mean velocities and the rms of velocity fluctuations in this case, although direct comparisons were not made for particle statistics.

The present study describes an Eulerian-Lagrangian approach, based on a RANS model coupled to a Lagrangian particle tracking (LPT) technique, and applies it in determining the dispersion characteristics of gas-solid flows, for a range of Stokes numbers, through a duct with a  $90^\circ$  bend. Compared to the previous studies noted above, the present work consistently applies an anisotropic approach to predicting both time-averaged turbulence velocities in the RANS model, and instantaneous velocities in the dispersion model. The present study also uses full three-dimensional tracking of particles within the flow, with significantly increased numbers of particles tracked in order to provide reliable particle statistics. The model described is subsequently validated using data obtained by Kliafas and Holt (1987) in a vertical-to-horizontal flow through a  $90^\circ$  bend which considered particle sizes of 50 and 100  $\mu\text{m}$ .

## 2. Mathematical model

### 2.1 Eulerian approach for the continuous phase

The Eulerian approach was based on solving the partial differential equations which describe the conservation of mass and momentum for three-dimensional, turbulent, unsteady, incompressible and isothermal flows in the absence of buoyancy. The mass and momentum conservation equations, expressed in time-averaged Cartesian tensor form, are given respectively as:

$$\frac{\partial \bar{u}_i}{\partial x_i} = 0 \quad (1)$$

$$\bar{u}_j \frac{\partial \bar{u}_i}{\partial x_j} = -\frac{1}{\rho} \frac{\partial \bar{P}}{\partial x_i} + \frac{\partial}{\partial x_j} \left[ \nu \left( \frac{\partial \bar{u}_i}{\partial x_j} + \frac{\partial \bar{u}_j}{\partial x_i} \right) - \overline{u'_i u'_j} \right] \quad (2)$$

Here, the variables in the instantaneous forms of the transport equations have been decomposed into mean and fluctuating quantities, and the resulting equations time-averaged. Mean values are denoted by an overbar, and fluctuating quantities by a prime, with  $u_i$  the three components of velocity in the corresponding  $x_i$  directions,  $t$  is time,  $\rho$  is the density,  $P$  the pressure and  $\nu$  the kinematic viscosity. The Reynolds stress term in Eq. (2) is unknown and must be expressed in terms of known quantities using a turbulence closure before these equations can be solved.

The equation set was closed using the second-moment turbulence closure of Jones and Musonge (1988), with the Reynolds stresses obtained directly from solutions of modelled partial differential transport equations. Following Jones and Musonge (1988), the closure may be specified as:

$$\frac{\partial \overline{u'_i u'_j}}{\partial t} + \bar{u}_j \frac{\partial}{\partial x_j} (\overline{u'_i u'_j}) = - \left( \overline{u'_i u'_l} \frac{\partial \bar{u}_j}{\partial x_l} + \overline{u'_j u'_l} \frac{\partial \bar{u}_i}{\partial x_l} \right) + C_s \frac{\partial}{\partial x_l} \left[ \frac{k}{\varepsilon} \overline{u'_l u'_m} \frac{\partial}{\partial x_m} (\overline{u'_i u'_j}) \right] + A_{ij} - \frac{2}{3} \delta_{ij} \varepsilon \quad (3)$$

where  $k$  is the turbulence kinetic energy and  $\varepsilon$  its dissipation rate. The redistributive fluctuating pressure term,  $A_{ij}$ , is modelled (Jones and Musonge, 1988; Dianat et al, 1996) as:

$$\begin{aligned} A_{ij} = & -C_1 \frac{\varepsilon}{k} (\overline{u'_i u'_j} - \frac{2}{3} k \delta_{ij}) + C_2 \delta_{ij} \overline{u'_l u'_m} \frac{\partial \bar{u}_l}{\partial x_m} + C_3 \left( \overline{u'_l u'_j} \frac{\partial \bar{u}_i}{\partial x_l} + \overline{u'_l u'_i} \frac{\partial \bar{u}_j}{\partial x_l} \right) + C_4 k \left( \frac{\partial \bar{u}_i}{\partial x_j} + \frac{\partial \bar{u}_j}{\partial x_i} \right) \\ & + C_5 \overline{u'_i u'_j} \frac{\partial \bar{u}_l}{\partial x_l} - \left( \frac{3}{2} C_2 + C_3 \right) \left( \overline{u'_l u'_j} \frac{\partial \bar{u}_l}{\partial x_i} + \overline{u'_l u'_i} \frac{\partial \bar{u}_j}{\partial x_l} \right) - \left( \frac{2}{3} C_4 + C_3 \right) k \delta_{ij} \frac{\partial \bar{u}_l}{\partial x_l} \end{aligned} \quad (4)$$

where  $\delta_{ij}$  is the Kronecker delta. Eq. (4) models  $A_{ij}$  as a general linear function of the Reynolds stress tensor under the assumption that the “return” and mean strain (or “rapid”) contributions to the velocity-pressure gradient correlation, normally modelled separately, are directly influenced by

mean strain. The model constants were taken as standard (Dianat et al, 1996), with  $C_5 = 0.22$ ,  $C_1 = 3.0$ ,  $C_2 = -0.44$ ,  $C_3 = -0.46$ ,  $C_4 = -0.23$  and  $C_5 = 0.3$ .

The turbulence kinetic energy dissipation rate required for solution of Eq. (3) was obtained, according to (Jones and Musonge, 1988; Dianat et al, 1996), from:

$$\frac{\partial \varepsilon}{\partial t} + \bar{u}_j \frac{\partial \varepsilon}{\partial x_j} = C_\varepsilon \frac{\partial}{\partial x_l} \left( \frac{k}{\varepsilon} \overline{u'_l u'_m} \frac{\partial \varepsilon}{\partial x_m} \right) - C_{\varepsilon 1} \frac{\varepsilon}{k} \overline{u'_l u'_m} \frac{\partial \bar{u}_l}{\partial x_m} - C_{\varepsilon 2} \frac{\varepsilon^2}{k} \quad (5)$$

where the constants in Eq. (5) were again taken as standard (Dianat et al, 1996), with  $C_\varepsilon = 0.18$ ,  $C_{\varepsilon 1} = 1.44$  and  $C_{\varepsilon 2} = 1.90$ .

## 2.2 Lagrangian approach for the dispersed phase

The flow regime considered, in line with the experimental measurements of Kliafas and Holt (1987), is a dilute suspension which occurs at very low particle volume fractions,  $\alpha_p < 10^{-6}$ . In such flows, the momentum transfer from the particles to the fluid flow has an insignificant effect on the flow, referred to as one-way coupling, and the standard method used to model such cases is to solve the fluid phase and subsequently integrate the particle equation of motion. In this approach, particle inertia and gravity are not accounted for in the fluid velocities seen by the particles, but are accounted for in the particle equation of motion.

The equations of motion for the computation of heavy particle ( $\rho/\rho_p \ll 1$ ) velocity,  $\vec{u}_p = (u_p, v_p, w_p)$ , and position,  $\vec{x}_p = (x_p, y_p, z_p)$ , vectors in the absence of particle rotation are given in the Lagrangian reference frame as:

$$\frac{d\vec{u}_p}{dt} = \frac{1}{\tau_p} (\vec{u} - \vec{u}_p) + \vec{g} \left( 1 - \frac{\rho}{\rho_p} \right) + \frac{\vec{F}_{sl}}{m_p} \quad (6)$$

$$\frac{d\vec{x}_p}{dt} = \vec{u}_p \quad (7)$$

where the subscript p designates the particle phase,  $m_p$  is the mass of a spherical particle,  $g$  gravitational acceleration and  $\vec{u} = (u, v, w)$  is the fluid velocity at the particle position. This velocity is determined as the sum of the fluid mean velocity obtained from the RANS solution following spatial interpolation, and the fluid velocity fluctuation calculated using the random Fourier series particle dispersion model described further below. The term on the left hand side of Eq. (6) denotes the inertia force acting on a particle due to its acceleration, whilst the terms on the right hand side represent drag, gravity/buoyancy and shear lift forces, respectively, and  $\tau_p$  is given by:

$$\tau_p = \frac{\rho_p d_p^2}{18\mu f_D} \quad (8)$$

where  $d_p$  is the particle diameter,  $\mu$  the fluid dynamic viscosity, and  $f_D$  is the drag factor which, together with the particle Reynolds number  $Re_p = d_p \rho |\bar{u} - \bar{u}_p| / \mu$ , is used to compute the drag coefficient  $C_D = 24f_D / Re_p$ . Among the many expressions for  $f_D$  which can be found in the literature, the following are the most common (Brenn et al, 2003) and are used in the present study:

$$\begin{aligned} f_D &= 1 & Re_p &\leq 0.2 \text{ Stokes law region} \\ f_D &= \left(1 + 0.1 Re_p^{0.99}\right) & 0.2 < Re_p &\leq 2 \\ f_D &= \left(1 + 0.11 Re_p^{0.81}\right) & 2 < Re_p &\leq 21 \\ f_D &= \left(1 + 0.189 Re_p^{0.632}\right) & 21 < Re_p &\leq 200 \\ f_D &= \left(1 + 0.15 Re_p^{0.687}\right) & 200 < Re_p &\leq 1000 \text{ Schiller \& Nauman drag law} \\ f_D &= 0.44 \times Re_p / 24 & 1000 < Re_p &\leq 2 \times 10^4 \text{ Newton's law region} \\ f_D &= 0.1 \times Re_p / 24 & Re_p &> 2 \times 10^5 \end{aligned} \quad (9)$$

The slip-shear lift force implemented is the Saffman lift, with the shear lift coefficient,  $C_{sl}$ , included to account for high Reynolds numbers:

$$\bar{F}_{sl} = \frac{1}{8} \pi \rho d_p^3 C_{sl} [(\bar{u} - \bar{u}_p) \times \bar{\omega}] \quad (10)$$

where  $\bar{\omega} = 0.5 \nabla \times \bar{u}$  is the fluid rotation, and  $C_{sl}$  is given as:

$$C_{sl} = \frac{4.1128}{Re_{sl}^{0.5}} f(Re_p, Re_{sl}) \quad (11)$$

$$f(Re_p, Re_{sl}) = \begin{cases} (1 - 0.3314 \beta^{0.5}) \exp(-0.1 Re_p) + 0.3314 \beta^{0.5} & : Re_p \leq 40 \\ 0.0524 (\beta Re_p)^{0.5} & : Re_p > 40 \end{cases} \quad (12)$$

where  $\beta = 0.5 Re_{sl} / Re_p$  and  $Re_{sl} = \rho d_p^2 |\bar{\omega}| / \mu$ .

### 2.3 Turbulence-induced particle dispersion

The instantaneous fluid velocity seen by the particles, i.e.  $u = \bar{u} + u'$ , required in the force terms was computed from the summation of time-averaged fluid velocities, obtained from the Eulerian solution, and fluctuating velocities. The fluctuating fluid velocities seen by the particle are not known from the RANS solution but were determined using a stochastic method based on a random Fourier series approach (Fan et al, 1997). This method has been successfully applied in a variety

of flows, e.g. Fan et al. (1997a, 1997b, 2002), Adams et al. (2011), Njobuenwu et al. (2009, 2012) and Njobuenwu and Fairweather (2012) and is reproduced here as:

$$\begin{aligned}
u' &= \sum_{i=1}^N \gamma_1 U_{m,i} \cos(\omega_i \Delta t - \gamma_2 \alpha_{u,i}) \\
v' &= \sum_{i=1}^N \gamma_3 V_{m,i} \cos(\omega_i \Delta t - \gamma_4 \alpha_{v,i}) \\
w' &= \sum_{i=1}^N \gamma_5 W_{m,i} \cos(\omega_i \Delta t - \gamma_6 \alpha_{w,i})
\end{aligned} \tag{13}$$

where  $\gamma_1 - \gamma_6$  are normal distribution random numbers (dimensionless),  $U_m$ ,  $V_m$  and  $W_m$  ( $\text{m s}^{-1}$ ) are fluctuation amplitudes based on the angular frequency,  $\omega=2\pi f$  ( $\text{rad s}^{-1}$ ), which were obtained from the fluctuation spectrum and turbulence energy, and  $f$  is the frequency (Hz) chosen to give a Gaussian distribution with a standard deviation of unity in  $\omega$ .  $\alpha_u$ ,  $\alpha_v$  and  $\alpha_w$ , (rad) are the initial fluctuating phases of the  $u$ ,  $v$  and  $w$  fluctuating velocities, respectively, which are randomly sampled between 0 and  $2\pi$ ,  $\Delta t$  (s) is the time step, such that the product  $\omega\Delta t$  ( $=2\pi f\Delta t$ ) has the dimensions (rad).  $N$  ( $= 10$ ) is the number of terms considered in the series. The amplitudes of fluctuation,  $U_m$ ,  $V_m$  and  $W_m$ , are obtained as a function of the turbulence energy spectrum,  $E$ , according to:

$$\begin{aligned}
U_{m,i}^2 &= E_i \overline{u'u'} \\
V_{m,i}^2 &= E_i \overline{v'v'} \\
W_{m,i}^2 &= E_i \overline{w'w'}
\end{aligned} \tag{14}$$

where  $E_i$  is the energy distribution ratio with respect to the frequency given (Fan et al, 1997b) by:

$$E_i = \frac{\int_{K_i}^{K_{i+1}} E(K) dK}{\int_0^{\infty} E(K) dK} \tag{15}$$

The turbulence energy spectrum  $E(K)$  used was that measured by Laurence (1956) for a jet and applied by Fan et al (1997) as:

$$E(K) = 16 \left( \frac{2}{\pi} \right)^{1/2} K^4 \exp(-2K^2) \tag{16}$$

where  $K$  is the wave number. Clearly other prescriptions for the energy spectrum could have been employed, although given that Eq. (16) has been applied to jet, pipe and duct flows (Fan et al. 1997a, 1997b, 2002) with some success it was retained in the present work.

## 2.4 Particle wall interactions

The Lagrangian tracking routine tracks particle trajectories before and after particles collide with a boundary wall. A particle collides with a boundary when its centre is one radius from the wall and it loses a fraction of its momentum before it is introduced back into the bulk flow. The momentum

change is expressed as a function of the coefficient of restitution,  $e$ , which is the ratio of particle velocity components after impingement to the corresponding components before impingement (Crowe et al, 1998). Grant and Tabakoff (1975) performed experiments in a wind tunnel using sand particles impinging on an aluminium surface ( $d_p=200 \mu\text{m}$ ,  $u=110\text{-}170 \text{ m s}^{-1}$ ) to obtain a stochastic particle rebound model formulated as least square fits to polynomial functions:

$$\begin{aligned} e_n &= 0.993 - 1.76\alpha - 1.56\alpha^2 + 0.49\alpha^3 \\ e_t &= 0.988 - 1.66\alpha - 2.11\alpha^2 + 0.67\alpha^3 \end{aligned} \quad (17)$$

where the subscripts  $n$  and  $t$  represent the normal and tangential directions, respectively, and  $\alpha$  is the particle impingement angle in radians.

The approach noted above was used in the present work. Additionally, and to model the effects of wall roughness, a stochastic approach called the “virtual wall” model (Sommerfeld, 1992; Sommerfeld and Huber, 1999; Crowe et al, 1998) was adopted. Here, the effective impact angle,  $\alpha$  used in Eq. (17), is assumed to be composed of the particle impact angle to a smooth wall,  $\alpha_1$ , and a stochastic contribution due to wall roughness,  $\Delta\gamma\xi$ : i.e.  $\alpha = \alpha_1 + \Delta\gamma\xi$ , where  $\xi$  is a Gaussian random number with zero mean and a standard deviation of unity. In this study, a wall roughness angle  $\Delta\gamma$  of  $3.8^\circ$  was used (Sommerfeld and Huber, 1999), corresponding to  $100 \mu\text{m}$  glass particles impinging on a Plexiglas surface.

### 3. Numerical solutions

#### 3.1 Boundary and initial conditions

Calculations were performed for the vertical-to-horizontal, square cross-section duct examined by Kliafas and Holt (1987). The computational domain was fully three-dimensional, with the duct having a side length ( $D$ ) of  $0.1 \text{ m}$  and a radius of bend curvature ( $R$ ) to bend width ratio ( $R/D$ ) of  $1.763$ . The duct starts  $10D$  upstream from the bend entrance and extends to  $12D$  downstream from the bend exit. A schematic representation of the computational domain and the coordinate system adopted is shown in Fig. 1. The streamwise direction shown in Fig. 1 is ( $z$ - $\theta$ - $x$ ), representing flow entering the duct, traversing the bend, and exiting the bend respectively. The corresponding transverse or radial direction is then ( $x$ - $r$ - $z$ ) respectively. The third spanwise direction is represented by  $y$  and is unchanged throughout the flow domain. In their experiments, Kliafas and Holt (1987) considered the motion of  $50$  and  $100 \mu\text{m}$  glass beads with a material density of  $2990 \text{ kg m}^{-3}$ . Bulk gas velocities of  $33.09$  and  $52.19 \text{ m s}^{-1}$ , corresponding to Reynolds numbers of  $2.2 \times 10^5$  and  $3.47 \times 10^5$ , were employed, with corresponding solid mass loadings of  $1.5 \times 10^{-4}$  and  $9.5 \times 10^{-5}$  and volumetric ratios of  $6.0 \times 10^{-8}$  and  $3.8 \times 10^{-8}$ . These authors used laser Doppler velocimetry to measure independently the first and second moments of gas and particle velocities at four locations within the bend, namely at  $0^\circ$ ,  $15^\circ$ ,  $30^\circ$  and  $45^\circ$ . These measured velocity profiles form the basis for the validation of the models developed in this study.

A non-uniform numerical solution mesh was employed such that the distribution of the grid nodes mimicked the velocity gradients present in the duct flow. The computational grid for every cross-section was generated using an algebraic grid generation function, with grid lines concentrated near all the walls using a power law stretching function (Tannehill et al, 1997). To accurately resolve the flow in the straight sections of the duct, the streamwise solution planes were clustered around the vicinity of the bend entrance and exit using a linear tangent stretching function. Hence, in the streamwise direction, the grid contracted from the inlet towards the bend in the upstream section, was uniform in the curved section of the bend, and expanded in the downstream section. In the transverse direction, the grid contracted from the bend centre-line towards the wall, allowing a finer dense mesh to be placed near solid surfaces. The computational domain also used a symmetry boundary down the central  $x$ - $z$  plane of the duct to reduce computer run times.

At the outlet of the duct the streamwise gradients of all variables were set to zero, with pressure taken as atmospheric. In line with the experimental study, mean velocities and turbulence levels at the inlet of the duct were specified as uniform, with:  $\bar{w} = W_b$ , the bulk inlet velocity, and  $\bar{u} = \bar{v} = 0$ ; turbulence kinetic energy,  $k = \frac{3}{2}(W_b I)^2$ , and its dissipation rate  $\varepsilon = C_\mu^{3/4} k^{1/2} l^{-1}$ , where  $C_\mu = 0.09$ ,  $I$  is the initial turbulence intensity, set to 1% of the bulk velocity,  $l$  is the turbulence length scale, given as  $l = 0.1 \times D$ ; and with the normal stresses  $\overline{u'u'} = \frac{1}{2}k$ ,  $\overline{v'v'} = \frac{2}{5}k$  and  $\overline{w'w'} = \frac{2}{3}k$  and shear stresses set to zero. For the grid nodes adjacent to the walls, the standard wall function method (Launder and Spalding, 1974) was applied.

The particle sizes used in the simulations were mono-dispersed, in line with the experiments of Kliafas and Holt (1987). The particles were distributed randomly across the inlet plane of the duct with initial velocities equal to those of the fluid at the particles' position.

### 3.2 Numerical solution methods

The fluid flow equations were solved using an existing computer program (Jones, 1991) based on body-fitted co-ordinates. The main feature of the code is that it involves the transformation of independent co-ordinates to a general curvilinear co-ordinate system in a way that the physical boundaries of the flow are coincident to the transformed co-ordinate lines. This procedure allows for complex geometries to be mapped to a rectangular volume, with the computations then carried out in the transformed domain using a square finite-volume mesh. The components of velocity are not transformed, and as a consequence are kept as dependent variables. All dependent variables, including the pressure, are stored at grid nodes and an implicit approximate factored pressure correction method is used to obtain finite-volume solutions to the flow equations. Central differencing is used for the diffusion terms, whilst convection terms are discretised using a bounded total variation diminishing scheme. The resulting system of quasi-linear equations is solved using pre-conditioned conjugate gradient methods. Overall, the method is second-order accurate in space and time. Further details can be found elsewhere (Jones, 1991).

For the particle equation of motion, each particle was tagged and assigned an initial position, generated from the stochastic sampling approach noted in the previous section. Fluid velocities at the centres of the particles, determined in computational space, were computed from the sum of the mean fluid velocities obtained from the Eulerian solution and the fluctuations obtained from the stochastic random Fourier series method. A fourth-order Runge-Kutta scheme (Neilson et al, 1997) was used to solve the particle equation of motion, Eqs. (6) and (7), to obtain the individual particle instantaneous velocity vector,  $\vec{u}_p$ , and the particle position vector,  $\vec{x}_p$ , at the end of a time interval  $\Delta t$  according to (Tu and Fletcher, 1995):

$$\vec{x}_p = \vec{x}_p^0 + 0.5 \times (\vec{u}_p + \vec{u}_p^0) \Delta t \quad (18)$$

where  $\vec{x}_p^0$  and  $\vec{u}_p^0$  are the particle initial position and velocity vectors. A particle's path  $\vec{x}_p$  was then tracked by continually updating its spatial position with time. If the particle was still in the solution domain, the next location of the particle was calculated, and the calculation procedure then repeated. If the new particle location was judged to be outside the solution domain, the particle had either struck a solid boundary or had left the computational domain across the exit plane. In the case of an impact, the impact point was determined first, and then the rebound velocity was calculated. With the impact position and the rebound velocity as the new set of initial conditions, trajectory calculations were then continued. If the rebound velocity was sufficiently small, the particle was assumed to have deposited on the wall. The particle tracker therefore performed five main tasks: particle location, interpolation, dispersion modelling, integration and particle wall collision modelling.

Fluid flow calculations were performed using three non-uniform grids of  $80 \times 40 \times 200$ ,  $120 \times 60 \times 200$  and  $160 \times 80 \times 200$ , representing nodes in the transverse, spanwise and streamwise directions respectively. As noted, and in order to reduce computational costs, only half of the duct geometry was modelled with a symmetry-plane boundary condition applied along the surface bisecting the duct. Hence, the number of grid nodes given for the duct width (in the spanwise direction) are for half of the duct width only. Numerical predictions of the fluid velocity profiles at the exit of the bend,  $\theta = 90^\circ$ , were used to establish grid independence. This position was chosen for testing because it accommodates the influences of streamline curvature due to the bend and the pressure gradient effects caused by the concave and convex bend walls. Analysis demonstrated that results from the  $120 \times 60 \times 200$  grid were not significantly changed by further refining the grid to  $160 \times 80 \times 200$ . Up to 250k particle trajectories were computed, with the results derived giving particle statistics which were independent of the number of particles employed.

## 4. Results and discussion

### 4.1 Fluid phase

Figure 2 shows the characteristic behaviour of turbulent fluid flow in a curved duct, with contours of the mean streamwise velocity  $\bar{w}$ , normalised by the bulk velocity  $W_b$ , and the pressure coefficient  $C_p$  given along the plane of symmetry ( $y/D = 0.5$ ) within the duct. Here, the pressure coefficient is defined as  $C_p = (P - P_{in}) / (0.5 \times \rho W_b^2)$ , where  $P$  is the local gas pressure and  $P_{in}$  the pressure at the inlet of the duct. This figure demonstrates the influence of the duct curvature on the flow, with the presence of the bend causing a non-uniform distribution of both the mean velocity and pressure in its vicinity. The symmetric flow in the vertical section of the duct, with the peak streamwise velocity at the duct centre and a near uniform pressure coefficient, is transformed as the flow approaches the bend, with the peak in the streamwise velocity shifting towards the inner radius of the bend as a result of the favourable pressure gradient, and with flow near the outer radius decelerating due to the unfavourable pressure gradient. As the flow advances further into the bend,  $0^\circ \leq \theta < 30^\circ$ , the streamwise velocity increases close to the inner radius wall, with the maximum streamwise velocity across the entire length of the duct occurring within this section of the bend. The developed velocity and pressure gradient then persist further into the bend,  $30^\circ \leq \theta \leq 90^\circ$ , with a subsequent reversal of the location of the peak velocity towards the outer bend radius, leading to a deceleration near the inner radius and an acceleration near the outer radius. The effect of the bend on the flow continues to distances significantly downstream of the bend, with the peak velocity remaining close to the outer wall of the duct at all distances shown in Fig. 2. Only at distances of the order of  $S/D > 12$  beyond the bend, where  $S$  is the length of the straight section of duct, does the flow return to normality and re-establish a symmetric velocity profile with a peak at the centre of the duct. This observation, that the bend influences fluid flow at upstream locations of up to  $S/D \approx 2$  and downstream distances of up to  $S/D \approx 12$ , has been noted previously in both experimental (Sudo et al, 2001) and numerical (Njobuenwu et al, 2009) studies.

Predictions of the gas phase, mean streamwise velocity profiles at the locations considered in the experiments of Kliafas and Holt (1987) are compared with data for the  $Re = 2.2 \times 10^5$  flow in Fig. 3(a) and for  $Re = 3.47 \times 10^5$  in Fig. 3(b). The dimensionless distance from the outer wall  $r^*$  used in this and subsequent figures is defined as  $r^* = (r - r_o) / (r_i - r_o)$ , where  $r_o$  and  $r_i$  are the outer and inner duct radius, respectively. It is worthy of note that there have been a number of previous attempts to predict the streamwise mean and root-mean-square fluctuating velocity profiles in the flows measured by Kliafas and Holt (1987) using a variety of turbulence models embedded within a RANS modelling framework (Tu and Fletcher, 1995; Chen, 2001; Niu, 2001; Ibrahim et al, 2006; Mohanaragam et al, 2007 and 2008; Tian et al, 2008). Whether by coincidence or choice, however, all these previous works have only attempted to predict the higher Reynolds number flow of Kliafas and Holt (1987) with, to the authors' knowledge, no publications on the prediction of the

lower Reynolds number flow. Additionally, no previous work has considered prediction of the mean and rms fluctuating velocities in the transverse direction.

For the high Reynolds number flow shown in Fig. 3(b) the model used in the present work successfully predicts the behaviour of the flow at the centre of the duct and in regions near its inner wall, thereby capturing the effects of flow curvature noted earlier. Some slight over-prediction of the mean velocity close to the inner wall does, however, occur at  $\theta=30^\circ$  and  $45^\circ$ . There is also a slight under-prediction of the velocity in the boundary layer on the outer wall of the bend at the same bend angles, with this under-prediction also observed in previous attempts to predict the same flow (Tu and Fletcher, 1995; Chen, 2001; Niu, 2001; Ibrahim et al, 2006; Mohanarangam et al, 2007 and 2008; Tian et al, 2008). These observations are also true for the lower Reynolds number flow, Fig. 3(a), although in this case the under-prediction on the outer wall of the duct is more pronounced and increases with streamwise position  $\theta$ . In addition, the over-prediction of data on the inner wall is more apparent, with the deviation from data again increasing with distance around the bend.

Figure 4 compares experimental and predicted mean transverse gas velocities in the bend section of the duct for both Reynolds number flows. Here, there is good agreement between the data and predictions of the present approach for both the Reynolds numbers considered. A positive transverse velocity is seen to occur only at the entrance to the bend ( $\theta=0^\circ$ ), with a negative velocity occurring at every other location within the bend. These negative velocities are again evidence of the redirection of the core flow from the inner radius of the bend towards its outer wall. At the bend entrance, the largest differences between data and predictions occur near the boundary layer on the inner convex wall, although these are small. Superior predictions are obtained at a bend angle of  $\theta=15^\circ$ , although by  $\theta=30^\circ$  the present approach slightly under-predicts the negative transverse velocity in the core region of the flow. This trend persists downstream, although unfortunately it is not possible to provide any model validation beyond  $\theta=45^\circ$  due to the absence of experimental data. Overall, therefore, although the model is able to provide acceptable qualitative and quantitative distributions of the transverse velocity for both Reynolds numbers, it does show some under-prediction of the secondary flows within the duct, with the magnitude of the under-prediction increasing through the bend.

Predictions of the rms streamwise and transverse fluctuating velocities are compared with experimental data in Figs. 5 and 6, respectively. Results for  $w_{rms}$  and  $u_{rms}$  in the bend section for both Reynolds numbers indicate that turbulence levels are relatively lower in the core region of the flow, but become considerably higher in the near-wall regions, as would be anticipated. Although the range of the data is limited in terms of its coverage of the duct width, and its proximity to the bend walls, the data show that peak  $w_{rms}$  values at both Reynolds numbers increase with distance around the bend on both the outer concave and inner convex surfaces, with the most significant increases occurring close to the outer wall. These trends are to some extent reproduced by the

predictions, although increases in turbulence levels on the outer wall in particular tend to be under-predicted at both Reynolds numbers, with agreement with data clearly superior for the  $Re=3.47\times 10^5$  case. In contrast, predictions of the transverse fluctuating velocity given in Fig. 6 are in closer accord with the measurements of Kliafas and Holt (1987). As expected,  $u_{rms}$  values are lower than their streamwise counterparts, with increases in  $u_{rms}$  with distance around the bend in this case only occurring close to the outer wall. Overall, predictions of  $w_{rms}$  and  $u_{rms}$  at the higher Reynolds number are in reasonable agreement with data, whilst at  $Re=2.2\times 10^5$  significant differences occur, particularly in the half of the duct bounded by the outer concave bend wall.

## 4.2 Particle phase

Particle trajectories were predicted using the developed three-dimensional Lagrangian particle tracker; hence, the full effects of the main streamwise and secondary flows within the duct were considered in calculating the trajectories. As previously noted, particle dispersion is controlled by both the instantaneous gas phase velocities and the particles' proximity to the wall boundaries. When a particle approaches a wall, it may or may not impact on the wall depending on the particle's inertia which is a function of its size. Small particles with low inertia are strongly influenced by the fluid velocity fluctuations and generally follow the mean fluid motion. The motion of larger particles, however, is dominated by their inertia, and particle-wall impaction is inevitable when a particle is within the neighbourhood of a solid surface.

The effect of particle size, and corresponding Stokes number, on particle behaviour and distribution within the  $90^\circ$  bend studied may be considered with reference to the results of Fig. 7. This figure shows, by way of illustration, trajectories for eight representative particles with diameters of 1, 50, 100 and 500  $\mu\text{m}$ . The trajectories of the smallest particles within the vertical, bend and horizontal sections of the computational domain are given in Fig. 7(a). These particles have a small relaxation time and Stokes number  $St\approx 0.0026$ , which implies that they follow the fluid flow as a tracer and with trajectories that correspond to the gas flow streamlines. The results of Fig. 7(a) do not show any evidence of particles rebounding from the wall; rather those close to the wall roll or slide on the wall surface. As the particle size and Stokes number increase the effects of inertia become significant, leading to the deviation of particle trajectories from the fluid flow streamlines. Figures 7(b) and 7(c) show that particles with diameters of 50 and 100  $\mu\text{m}$ , corresponding to  $St\approx 3.65$  and  $St\approx 11.85$  respectively, impact on the bend outer wall on one or two occasions. There are also some collisions on the outer wall of the horizontal section of the duct. However, the inertia of the particles with a diameter of 50  $\mu\text{m}$  is not large enough to cause them to impact both the outer wall of the bend and the inner wall of the straight horizontal duct section, although this does occur for the larger 100  $\mu\text{m}$  particles. By way of contrast, the largest 500  $\mu\text{m}$  diameter particles considered, with  $St\approx 205.95$ , shown in Fig. 7(d) have enough momentum and sufficiently high rebound velocities from frequent collisions with the outer bend wall that they continue to collide with both the inner and outer walls of the horizontal section of the duct as they move downstream.

Particle velocity results considered below are for the  $Re=2.2 \times 10^5$  flow with 50 and 100  $\mu\text{m}$  particles, and for the  $Re=3.47 \times 10^5$  case with  $d_p=50 \mu\text{m}$ . The effect of particle inertia on the dispersion characteristics of the  $Re=2.2 \times 10^5$  flow with  $d_p=50 \mu\text{m}$  is demonstrated in Fig. 8 which gives predictions of instantaneous particle dispersion patterns at different cross-sections in the duct. It should be noted that the duct is magnified 10 times in the spanwise direction in this figure for clarity of presentation, and the thickness of the cross-sectional planes is approximately one particle diameter. The uniform particle distribution at the inlet of the duct and upstream of the bend section is clear from this figure, although this evolves into a non-uniform distribution within and downstream of the bend. The formation of a non-uniform distribution with high concentrations close to the outer bend wall is known as particle roping, and its occurrence leads to a skewing of the initial particle volume fraction distribution with significant gradients in that quantity across the duct cross-section. Further details of the particle distribution at selected cross-sectional locations are presented in Fig. 9. Predicted time-averaged particle volume fraction,  $\alpha_p$ , profiles on the duct symmetry plane are shown in Fig. 10 for those angles around the bend at which subsequent velocity field comparisons are made, with the volume fraction plotted in terms of the dimensionless distance from the outer wall. A total number of 250k particles were used in deriving these results, with this number of particles giving an initial particle volume fraction of magnitude  $O(10^{-8})$  at the inlet plane of the duct. These results quantify the phenomena illustrated in Figs. 8 and 9, on the symmetry plane at least, and demonstrate peak volume fraction values occurring at distances from the outer wall ( $\alpha_{p,\text{max}}, r^*$ ) of  $(1.94 \times 10^{-7}, 0.44)$ ,  $(2.02 \times 10^{-7}, 0.38)$ ,  $(5.60 \times 10^{-7}, 0.063)$  and  $(2.64 \times 10^{-6}, 0.092)$  at  $\theta=0^\circ$ ,  $15^\circ$ ,  $30^\circ$  and  $45^\circ$ , respectively. Similar results were also found for the  $Re=2.2 \times 10^5$  flow with 100  $\mu\text{m}$  particles, and for the  $Re=3.47 \times 10^5$  case with  $d_p=50 \mu\text{m}$ . For  $\alpha_p \leq 10^{-6}$ , the fluid phase momentum can be considered independent of that of the solid phase, and hence one-way coupling between the phases can be assumed, as was done in the experiments of Kliafas and Holt (1987). The results of Fig. 10 would therefore appear to suggest that this assumption holds at all locations used below in comparisons between measured and predicted particle velocity statistics, apart from at  $\theta=45^\circ$  where the influence of particle roping may have impacted to some extent upon this assumption close to the outer wall of the bend.

Besides the particle dispersion and concentration, other important statistics are particle mean and rms of velocity fluctuations. As noted, Kliafas and Holt (1987) considered the motion of 50 and 100  $\mu\text{m}$  glass beads in the  $Re=2.2 \times 10^5$  flow, and 50  $\mu\text{m}$  particles in the  $Re=3.47 \times 10^5$  flow. Predicted mean and fluctuating particle velocities are compared with experimental data for all three cases below. In deriving these predictions, up to 250k computational particles were required to obtain statistical independence of the results. Mean and fluctuating particle velocities were derived by creating bins centred on the grid nodes used to solve the fluid flow equations to capture the particles' instantaneous velocities, with a running averaging method employed to compute the mean and rms of their velocity fluctuations. Mean values,  $\bar{\varphi}(r^*)$ , of particle velocity components were therefore evaluated from the instantaneous values  $\varphi(r^*)$  captured in the bins across each normalised transverse position ( $r^*$ ) using:

$$\bar{\varphi}(r^*) \approx \frac{1}{N} \sum_{n=1}^N \varphi(r^*) \quad (19)$$

where  $\varphi(r^*)$  is the  $n^{th}$  sample of the instantaneous velocity out of a total of  $N$  samples. A fluctuation about this mean is then defined as  $\varphi'(r^*) = \varphi(r^*) - \bar{\varphi}(r^*)$ , so that the rms of turbulent fluctuations  $\varphi(r^*)_{rms}$  is given by:

$$\varphi(r^*)_{rms} \approx \left[ \frac{1}{N} \sum_{n=1}^N \varphi'(r^*)^2 \right]^{\frac{1}{2}} \quad (20)$$

Figure 11 compares predictions of the particle mean streamwise velocities within the bend section with the experimental data for mono-dispersed particles of 50 and 100  $\mu\text{m}$  diameter, and for both flow Reynolds numbers, with the results showing good agreement between the predicted profiles and the data for both particle sizes. It is noteworthy that, in predicting these data, the particle-wall interaction model has, in general, handled the three-dimensional interactions between the particles and the outer wall of the bend reasonably well. However, there is some under-prediction of the particle mean velocities close to the concave wall of the bend at  $\theta=30^\circ$  and  $45^\circ$ , a trend also observed in previous work (Tu and Fletcher, 1995; Mohanarangam et al, 2007 and 2008), which may to some extent be due to inadequacies in the particle-wall interaction model and the particle roping observed in the predictions. However, mean gas velocities, given in Fig. 3, were also slightly under-predicted close to the outer duct wall at these measurement locations, particularly for the low Reynolds number case, and as a consequence this under-prediction also affects the particle velocity results. The under-prediction for particles of 50  $\mu\text{m}$  diameter at both Reynolds numbers starts at an angle of  $\theta=30^\circ$  (Fig. 11(a) and (c)), and at the same location for the 100  $\mu\text{m}$  diameter particles in the  $\text{Re}=2.2 \times 10^5$  flow (Fig. 11(b)), and appears to increase with bend angle. This likely occurs due to the large number of collisions that take place at this location, with agreement with data affected by inaccuracies that result from the summation of the velocities of particles that have and have not rebounded from the concave wall. In contrast, in the core of the flow and the boundary layer on the convex wall the predictions match the experimental data reasonably well.

Equivalent comparisons between predictions of the particle mean transverse velocities and experimental data are given in Fig. 12. In this case the predictions reproduce the experimental data, with good agreement obtained for both particle sizes and Reynolds numbers considered, even in regions at and beyond a bend angle of  $30^\circ$  where there is a notable increase in the particle velocity near the concave wall. Some under-prediction of the data is apparent for the 50  $\mu\text{m}$  particles at  $\theta=45^\circ$  and for  $r^* \approx 0.15$ , where a sharp transition in the predictions contrasts with a smoother change in the data. Some under-prediction is also apparent in the core of the  $\text{Re}=2.2 \times 10^5$  flow for the same particles.

It is interesting to note that the gas phase, mean streamwise velocity profiles (Fig. 3) exhibit significantly more variation across the duct than those of the particles (Fig. 11) which, in contrast, are relatively flat. For the particle velocity profiles to mimic those of the fluid, the particle Stokes number should be less than unity. However, in this case the particles had diameters of 50 and 100  $\mu\text{m}$ , corresponding to  $St \approx 3.65$  and  $St \approx 11.85$ , respectively. These particles are therefore sufficiently large for their trajectory towards the bend to develop under the influence of gravity, with their behaviour within the bend itself less affected by that of the fluid and the pressure gradient encountered in this region of the flow. Consequently, no particles were observed experimentally or in the predictions between  $\theta = 15^\circ$  and  $45^\circ$  close to the inner wall of the duct. Overall, the mean particle velocity predictions are in good agreement with the data for the two particle sizes and Reynolds numbers considered and, despite the under-prediction of particle mean streamwise velocities close to the outer wall noted above for both particle sizes, the methods of generating instantaneous velocities from the RANS solutions and of treating particle-wall collisions appear to be capable of simulating particle dispersion in the duct. Additionally, predictions of the particle mean transverse velocities are in good agreement with data near both the concave and convex walls, as well as in the core of the flow. Although reasonable agreement between predictions and experimental data has been obtained previously by other authors for the streamwise mean velocity, in particular, using two-dimensional computations, the agreement obtained in the present work suggests that three-dimensional simulations are more effective and give superior results in predictions of what is clearly a three-dimensional flow.

Figure 13 shows predicted profiles of the rms of the particle fluctuating streamwise velocity component, again for two particle diameters and two Reynolds numbers, while Fig. 14 gives equivalent results in the transverse direction. The predictions in the streamwise direction show reasonable agreement with the data, although there is a notable reduction in the accuracy of the predictions for the lower Reynolds number flow when the smaller particles are replaced by their larger counterparts. Interestingly, however, and for the latter  $Re = 2.2 \times 10^5$  flow with the 100  $\mu\text{m}$  diameter particles, the experimental data do appear qualitatively different and out of step with the other measurements given in Fig. 13, and indeed with those of Figs. 5, 6 and 14. In the transverse direction, all calculated results show an under-prediction of the data for both Reynolds numbers and both particle sizes, although reasonable qualitative agreement is obtained. The largest discrepancy is again for the  $Re = 2.2 \times 10^5$  case with 100  $\mu\text{m}$  particles, with the under-prediction in all cases occurring despite the good agreement between measurements and predictions of the gas phase transverse velocity fluctuations. Observed disagreement between predictions and measurements close to the outer wall of the duct in Fig. 13 and 14 may again to some extent be due to inadequacies in the particle-wall interaction model, and the prediction of particle roping. However, and despite these discrepancies, these comparisons demonstrate that the anisotropic, random Fourier series approach to modelling particle dispersion does yield reasonable predictions of both the instantaneous fluid and particle velocities. This again contrasts with earlier studies (Naik

and Bryden, 1999; Niu, 2001; Mohanarangam et al, 2007) which used the stochastic approach of Gosman and Ioannides (1981), based on the assumption of isotropic turbulence, to model particle dispersion, with Mohanarangam et al (2007) in particular reporting that their approach could not quantitatively predict particle velocity fluctuations.

## 5. Conclusions

This work has used an Eulerian-Lagrangian approach, representing deterministic and stochastic modelling methods, to study the behaviour of gas-solid flows in a square cross-section duct with a 90° bend. The Eulerian approach was based on a RANS modelling framework closed using a second-moment turbulence model, while the Lagrangian approach was based on the solution of the particle equation motion, with particle dispersion modelled using a stochastic approach that ensured turbulence anisotropy in the flow field predictions. One-way coupling between the particles and the fluid flow was assumed, in line with the experiments used for model validation, since predictions demonstrated that an initial particle volume fraction of  $O(10^{-8})$  evolved to  $O(10^{-6})$ , only slightly exceeding the latter magnitude at 45° around the bend and close to its outer wall. Two-way and/or four-way coupling between the fluid flow and particles might be usefully employed in the future to more accurately resolve fluid-particle momentum transfer in regions where the particle concentration is high.

The behaviour of the gas phase has been demonstrated to be characterised by the pressure distribution within the duct. In particular, the movement of the peak velocity toward the inner wall of the duct in the first half of the bend, and towards the outer wall in the second half, is well predicted, demonstrating accurate representation of the effects of the centrifugal force on the flow characteristics. Detailed predictions of mean and fluctuating fluid and particle velocities have been validated by comparing model predictions at various angular displacements within the bend with experimental measurements (Kliafas and Holt, 1987) on dispersed gas-solid flows in a vertical-to-horizontal flow configuration. Reasonable agreement between the predictions and experimental data for both gas and particle phases confirm the appropriateness of the modelling techniques employed.

In all the predictions presented, results for the higher Reynolds number ( $Re=3.47 \times 10^5$ ) flow, for both gas and particle phases, show better agreement with data when compared to the predictions of the lower Reynolds number ( $Re=2.20 \times 10^5$ ) case. It is notable that previous works that also considered the test case examined in the present work only compared predictions with the higher Reynolds number case, with no comparisons available for the  $Re=2.20 \times 10^5$  flow. Additionally, and again unlike previous works, the present approach provides reasonable predictions of particle fluctuating velocities within the flows.

Overall, the results demonstrate that the modelling approaches developed compare favourably with those of other authors, noted in the introduction, in terms of their ability to predict particle-laden

flows through duct bends, and provide a firm basis for the further development of more accurate methods of handling such flows. Differences between the present work and that of other authors lie mainly in the consistent application of an anisotropic approach to predicting time-averaged turbulence velocities in the RANS model, and instantaneous velocities in the dispersion model. The present study also demonstrates the advantage of three- over two-dimensional particle tracking techniques in the prediction of particle dispersion, thereby accommodating particles which cross the central plane of the duct and the impact they have on the predictions, with the associated and necessary increase in the number of particles tracked in the present work also likely responsible for some of the improvement in the predicted particle statistics.

Lastly, it is noteworthy that the dispersion model employed does not account for the influence of the fluid shear Reynolds stresses, and the use of more elaborate approaches (Berlemont et al., 1990; Zhou and Leschziner, 1991; Burry and Bergeles, 1993) which use both the normal and shear stresses seen by a particle to give values for the instantaneous fluid velocities is worthy of further investigation.

#### **Acknowledgement**

The authors would like to thank the Commonwealth Scholarship Commission in the United Kingdom for supporting D.O. Njobuenwu's research.

## References

- Adams, J.F.W., Fairweather, M., Yao, J., 2011. Modelling and simulation of particle re-suspension in a turbulent square duct flow. *Compt. Chem. Eng.* 35, 893-900.
- Armenio, V., Fiorotto, V., 2001. The importance of the forces acting on particles in turbulent flows. *Phys. Fluids* 13, 2437-2440.
- Berlemont, A., Desjonquieres, P., Gouesbet, G., 1990. Particle Lagrangian simulation in turbulent flows. *Int. J. Multiphase Flow* 16, 19-34.
- Brenn, G., Braeske, H., Zivkovic, G., Durst, F., 2003. Experimental and numerical investigation of liquid channel flows with dispersed gas and solid particles. *Int. J. Multiphas. Flow* 29, 219-247.
- Burry, D., Bergeles, G., 1993. Dispersion of particles in anisotropic turbulent flows. *Int. J. Multiphase Flow* 19, 651-664.
- Chen, X., 1997. Efficient particle tracking algorithm for two-phase flows in geometries using curvilinear coordinates. *Numer. Heat Tr. A-Appl.* 32, 387-405.
- Chen, X.Q., 2001. Multigrid acceleration of computations of turbulent particle-laden flows. *Numer. Heat Tr. B-Fund.* 40, 139-162.
- Crowe, C.T., Sommerfeld, M., Tsuji, Y., 1998. *Multiphase flows with droplets and particles*, CRC Press, Boca Raton, Florida.
- Crowe, C.T., Troutt, T.R., Chung, J.N., 1996. Numerical models for two-phase turbulent flows. *Annu. Rev. Fluid Mech.* 28, 11-43.
- Dianat, M., Fairweather, M., Jones, W.P., 1996. Reynolds stress closure applied to axisymmetric, impinging turbulent jets. *Theor. Comp. Fluid Dyn.* 8, 435-447.
- Fan, J.R., Yao, J., Cen, K.F., 2002. Antierosion in a 90 degrees bend by particle impaction. *AIChE J.* 48, 1401-1412.
- Fan, J.R., Zhang, X.Y., Chen, L.H., Cen, K.F., 1997a. New stochastic particle dispersion modeling of a turbulent particle-laden round jet. *Chem. Eng. J.* 66, 207-215.
- Fan, J.R., Zhang, X.Y., Cheng, L.H., Cen, K.F., 1997b. Numerical simulation and experimental study of two-phase flow in a vertical pipe. *Aerosol Sci. Technol.* 27, 281-292.
- Gosman, A.D., Ioannides, E., 1981. Aspects of computer simulation of liquid-fuelled combustors. American Institute of Aeronautics and Astronautics, 19<sup>th</sup> Aerospace Sciences Meeting, St Louis, MO, USA, AIAA Paper 81-0323.
- Gouesbet, G., Berlemont, A., 1999. Eulerian and Lagrangian approaches for predicting the behaviour of discrete particles in turbulent flows. *Prog. Energy Combust. Sci.* 25, 133-159.
- Grant, G., Tabakoff, W., 1975. Erosion prediction in turbomachinery resulting from environmental solid particles. *J. Aircraft* 12, 471-478.
- Grigoriadis, D.G.E., Kassinos, S.C., 2009. Lagrangian particle dispersion in turbulent flow over a wall mounted obstacle. *Int. J. Heat Fluid Flow* 30, 462-470.
- Ibrahim, K.A., El-Kadi, M.A., Hamed, M.H., El-Behery, S.M., 2006. Gas-solid two-phase flow in 90° bend. *Alexandria Eng. J.* 45, 417-433.

- Jones, W.P., 1991. BOFFIN: A computer program for flow and combustion in complex geometries. Department of Mechanical Engineering, Imperial College of Science, Technology and Medicine, London, UK.
- Jones, W.P., Musonge, P., 1988. Closure of the Reynolds stress and scalar flux equations. *Phys. Fluids* 31, 3589-3604.
- Kliafas, Y., Holt, M., 1987. LDV measurements of a turbulent air-solid two-phase flow in a 90° bend. *Exp. Fluids* 5, 73-85.
- Kuan, B., William, Y., Solnordal, C., 2003. CFD simulation and experimental validation of dilute particulate turbulent flow in 90° duct bend. *Proc. 3<sup>rd</sup> International Conference on CFD in the Minerals and Process Industries*, CSIRO, Melbourne, Australia, 531-536.
- Kuan, B., Yang, W., Schwarz, M.P., 2007. Dilute gas-solid two-phase flows in a curved 90° duct bend: CFD simulation with experimental validation. *Chem. Eng. Sci.* 62, 2068-2088.
- Launder, B.E., Spalding, D.B., 1974. Numerical computation of turbulent flows. *Comput. Method. Appl. M.* 3, 269-289.
- Laurence, J.C., 1956. Intensity, scale, and spectra of turbulence in mixing region of free subsonic jet. *NACA Report No. 1292*.
- Mohanarangam, K., Tian, Z.F., Tu, J.Y., 2007. Numerical computation of turbulent gas-particle flow in a 90 degree bend: Comparison of two particle modelling approaches. *ANZIAM J* 48, C741-C758.
- Mohanarangam, K., Tian, Z.F., Tu, J.Y., 2008. Numerical simulation of turbulent gas-particle flow in a 90 degree bend: Eulerian-Eulerian approach. *Comput. Chem. Eng.* 32, 561-571.
- Naik, S., Bryden, I.G., 1999. Prediction of turbulent gas-solids flow in curved ducts using the Eulerian-Lagrangian method. *Int. J. Numer. Meth. Fl.* 31, 579-600.
- Nielson, G., Hagen, H., Muller, H., 1997. *Scientific visualization: overviews, methodologies, and techniques*. IEEE Computer Society, Los Alamitos, California.
- Niu, Y.Y., 2001. Evaluation of erosion in a two-way coupled fluid-particle system. *Int. J. Numer. Meth. Fl.* 36, 711-742.
- Njobuenwu, D.O., Fairweather, M., Yao, J., 2012. Prediction of turbulent gas-solid flow in a duct with a 90° bend using an Eulerian-Lagrangian approach. *AIChE J.* 58, 14-30.
- Njobuenwu, D.O., Fairweather, M., 2012. Modelling of pipe bend erosion by dilute particle suspensions. *Compt. Chem. Eng.* 42, 235-247.
- Njobuenwu, D.O., Fairweather, M., Yao, Y., 2009. Prediction of gas-solid flows in a square duct with a 90° bend. In: Hanjalić, K., Nagano, Y., Jakirlić, S. (Eds.), *Proc. Sixth International Symposium on Turbulence, Heat and Mass Transfer*, Begell House Inc., New York, pp. 769-772.
- Sommerfeld, M., 1992. Modelling of particle-wall collisions in confined gas-particle flows. *Int. J. Multiphase Flow* 18, 905-926.
- Sommerfeld, M., 2003. Analysis of collision effects for turbulent gas-particle flow in a horizontal channel: Part 1. Particle transport. *Int. J. Multiphas. Flow* 29, 675-699.
- Sommerfeld, M., Huber, N., 1999. Experimental analysis and modelling of particle-wall collisions. *Int. J. Multiphas. Flow* 25, 1457-1489.

Sudo, K., Sumida, M., Hibara, H., 2001. Experimental investigation on turbulent flow in a square-sectioned 90-degree bend. *Exp. Fluids* 30, 246-252.

Tannehill, J.C., Anderson, D.A., Pletcher, R.H., 1997. *Computational fluid mechanics and heat transfer*, 2<sup>nd</sup> edition, Taylor & Francis, Washington DC.

Tian, Z.F., Inthavong, K., Tu, J.Y., Yeoh, G.H., 2008. Numerical investigation into the effects of wall roughness on a gas-particle flow in a 90° bend. *Int. J. Heat Mass Tran.* 51, 1238-1250.

Tsuji, Y., Morikawa, Y., Tanaka, T., Nakatsukasa, N., Nakatani, M., 1987. Numerical simulation of gas solid two-phase flow in a two-dimensional horizontal channel. *Int. J. Multiphas. Flow* 13, 671-684.

Tu, J.Y., Fletcher, C.A.J., 1995. Numerical computation of turbulent gas-solid particle flow in a 90-degree bend. *AIChE J.* 41, 2187-2197.

Zhou, Q., Leschziner, M.A., 1991. A time-correlated stochastic model for particle dispersion in anisotropic turbulence. *Proc. 8<sup>th</sup> Symposium on Turbulent Shear Flows*. Munich, Germany, Vol. 1, 10-3-1 to 10-3-6.

## Figure Legends

- Figure 1. Schematic representation of computational domain and coordinate system.
- Figure 2. Flow development in duct bend: contours showing distribution of streamwise mean velocity and pressure coefficient.
- Figure 3. Measured and predicted values of gas phase, mean streamwise velocities within bend for (a)  $Re=2.2 \times 10^5$  and (b)  $Re=3.47 \times 10^5$  ( $\circ$  measured, — predicted).
- Figure 4. Measured and predicted values of gas phase, mean transverse velocities within bend for (a)  $Re=2.2 \times 10^5$  and (b)  $Re=3.47 \times 10^5$  ( $\circ$  measured, — predicted).
- Figure 5. Measured and predicted values of gas phase, rms fluctuating streamwise velocities within bend for (a)  $Re=2.2 \times 10^5$  and (b)  $Re=3.47 \times 10^5$  ( $\circ$  measured, — predicted).
- Figure 6. Measured and predicted values of gas phase, rms fluctuating transverse velocities within bend for (a)  $Re=2.2 \times 10^5$  and (b)  $Re=3.47 \times 10^5$  ( $\circ$  measured, — predicted).
- Figure 7. Trajectories of eight particles in half of the duct for (a) 1  $\mu\text{m}$ , (b) 50  $\mu\text{m}$ , (c) 100  $\mu\text{m}$  and (d) 500  $\mu\text{m}$  particles.
- Figure 8. Predicted instantaneous particle dispersion patterns in the duct at various streamwise locations for  $Re=2.2 \times 10^5$  and  $d_p=50 \mu\text{m}$ .
- Figure 9. Snapshots of particle distribution predictions at selected locations (left to right, and top to bottom,  $\theta=0^\circ, 15^\circ, 30^\circ, 45^\circ, 60^\circ$  and  $90^\circ$ , and  $S/D = 1, 5$  and  $9$ ) for  $Re=2.2 \times 10^5$  and  $d_p=50 \mu\text{m}$ .
- Figure 10. Predicted particle volume fraction,  $\alpha_p$ , profiles on the duct symmetry plane for  $Re=2.2 \times 10^5$  and  $d_p=50 \mu\text{m}$ .
- Figure 11. Measured and predicted values of particle mean streamwise velocities within bend for (a)  $Re=2.2 \times 10^5$ ,  $d_p=50 \mu\text{m}$ , (b)  $Re=2.2 \times 10^5$ ,  $d_p=100 \mu\text{m}$  and (c)  $Re=3.47 \times 10^5$ ,  $d_p=50 \mu\text{m}$  ( $\circ$  measured, — predicted).
- Figure 12. Measured and predicted values of particle mean transverse velocities within bend for (a)  $Re=2.2 \times 10^5$ ,  $d_p=50 \mu\text{m}$ , (b)  $Re=2.2 \times 10^5$ ,  $d_p=100 \mu\text{m}$  and (c)  $Re=3.47 \times 10^5$ ,  $d_p=50 \mu\text{m}$  ( $\circ$  measured, — predicted).
- Figure 13. Measured and predicted values of particle rms fluctuating streamwise velocities within bend for (a)  $Re=2.2 \times 10^5$ ,  $d_p=50 \mu\text{m}$ , (b)  $Re=2.2 \times 10^5$ ,  $d_p=100 \mu\text{m}$  and (c)  $Re=3.47 \times 10^5$ ,  $d_p=50 \mu\text{m}$  ( $\circ$  measured, — predicted).
- Figure 14. Measured and predicted values of particle rms fluctuating transverse velocities within bend for (a)  $Re=2.2 \times 10^5$ ,  $d_p=50 \mu\text{m}$ , (b)  $Re=2.2 \times 10^5$ ,  $d_p=100 \mu\text{m}$  and (c)  $Re=3.47 \times 10^5$ ,  $d_p=50 \mu\text{m}$  ( $\circ$  measured, — predicted).

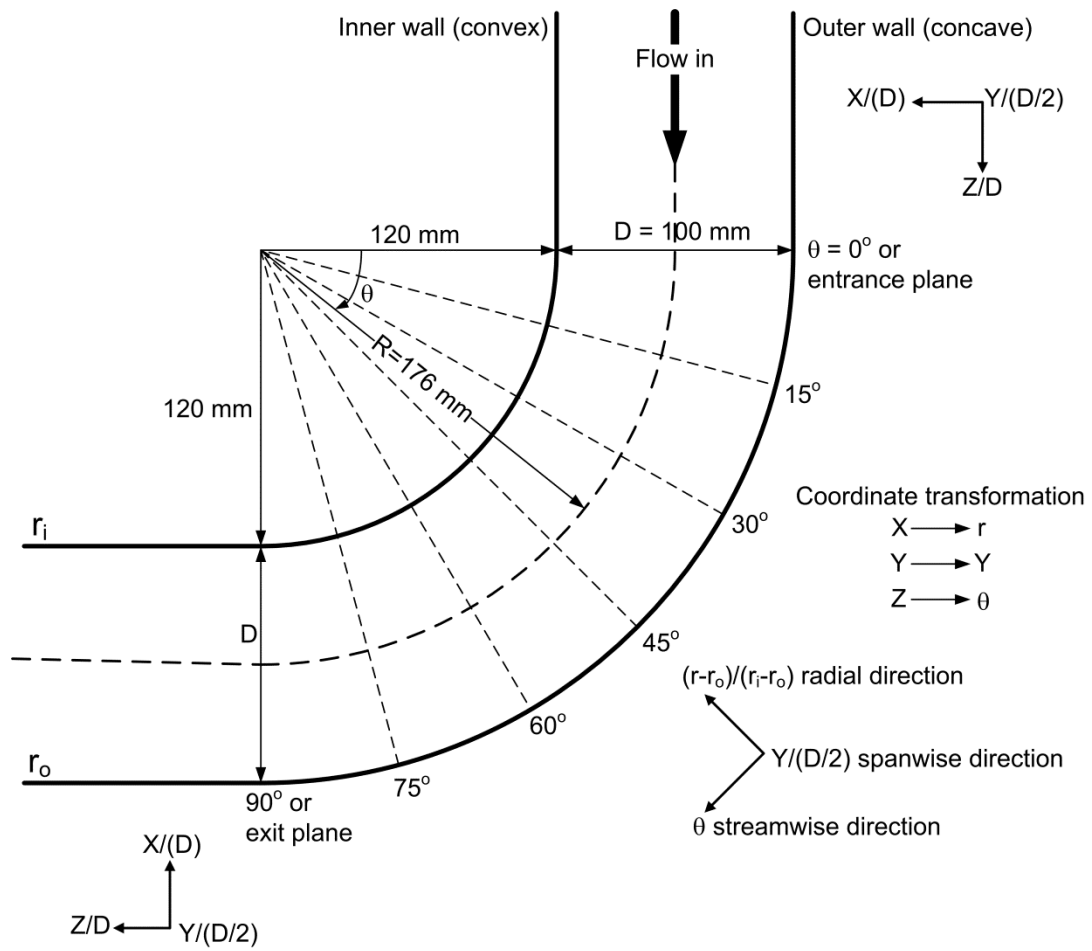


Figure 1

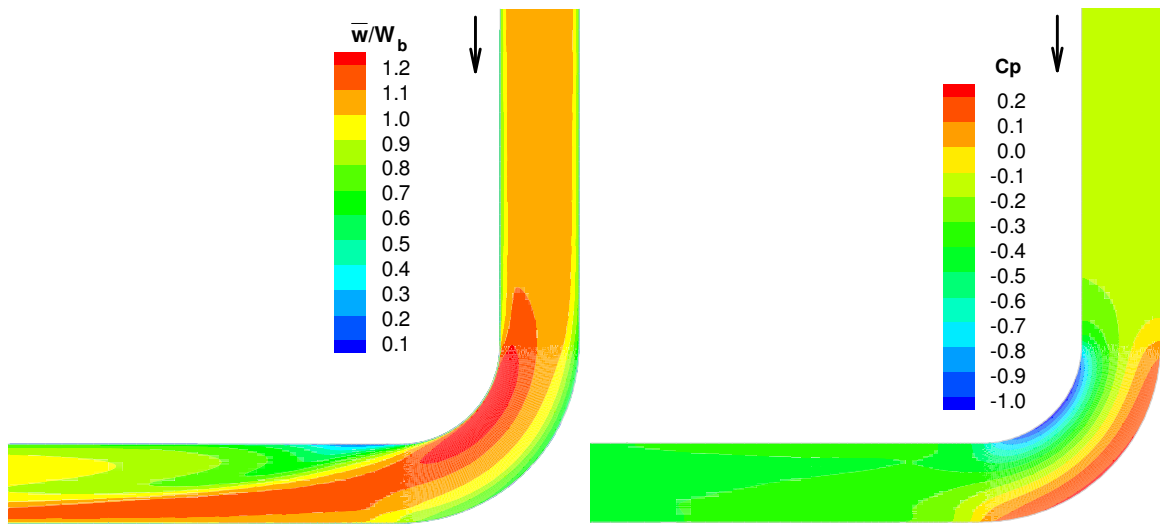


Figure 2

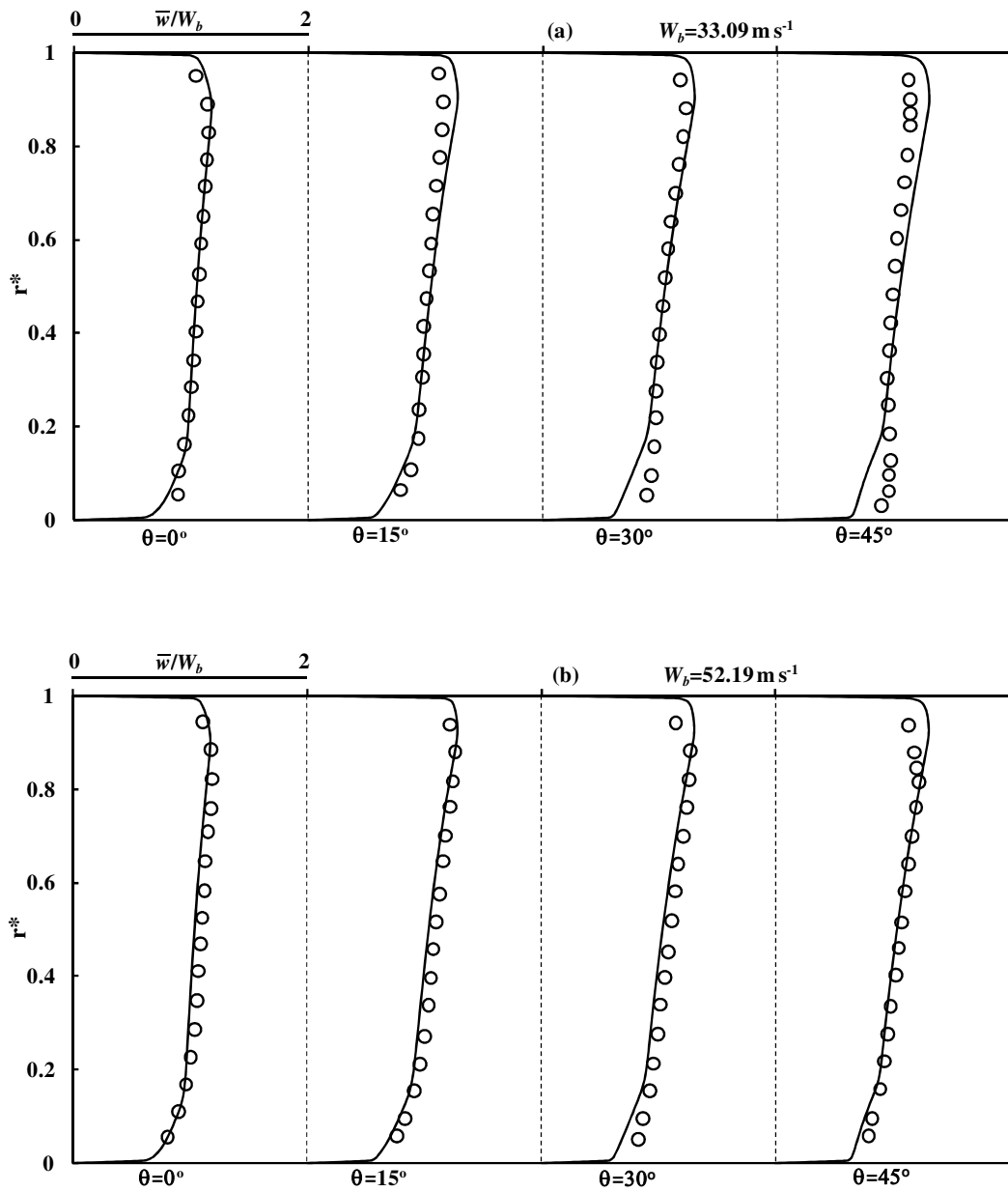


Figure 3

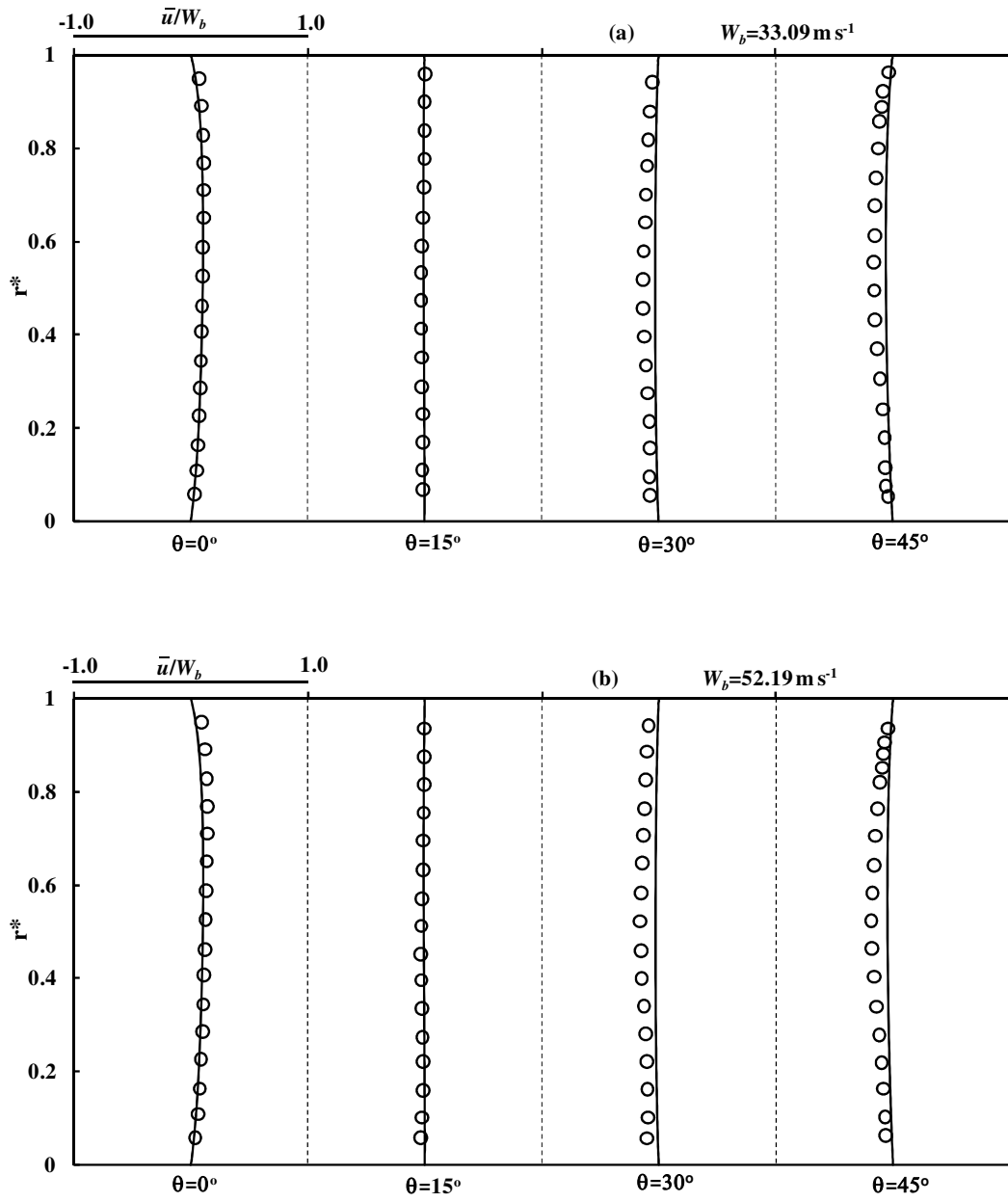


Figure 4

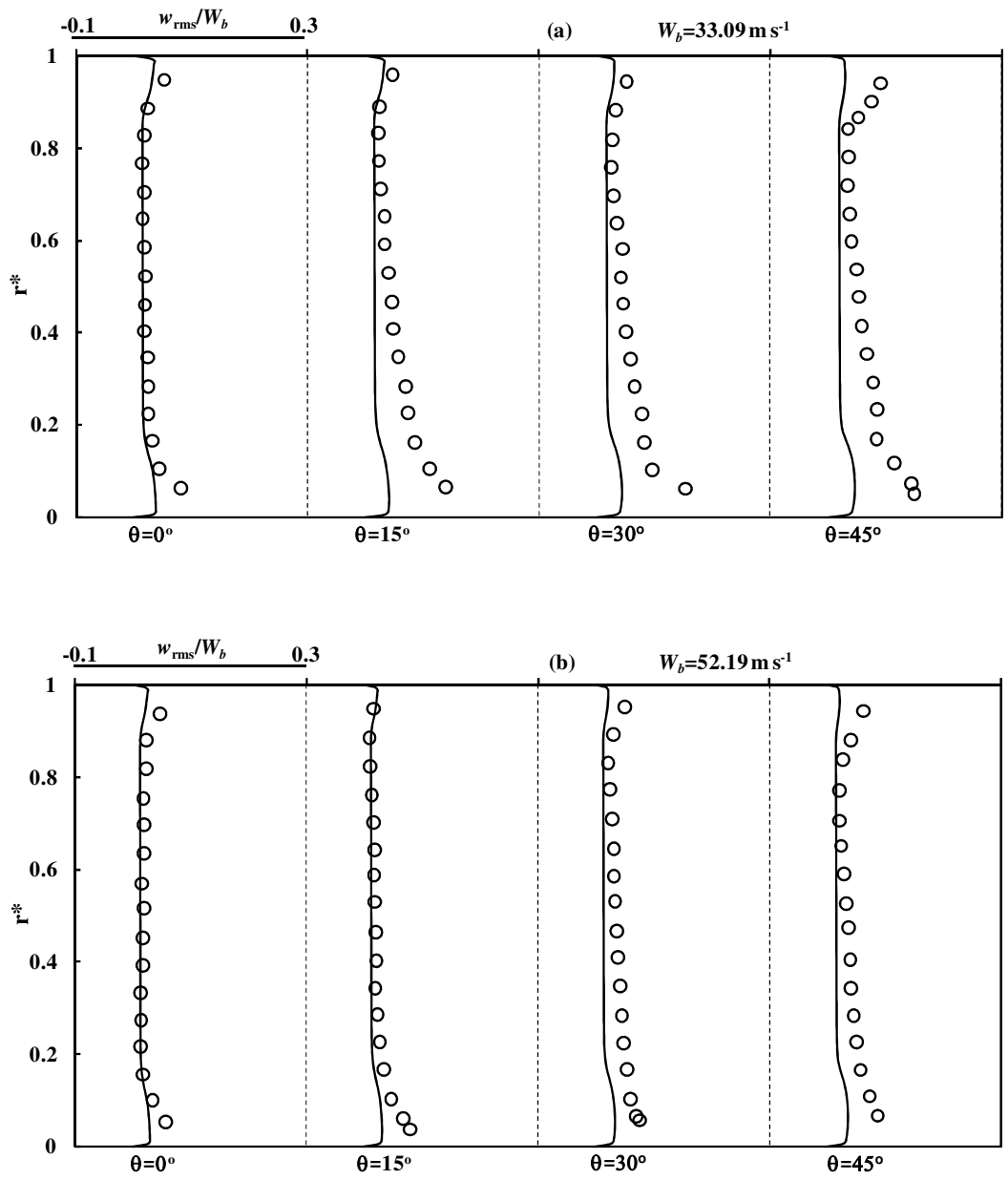


Figure 5

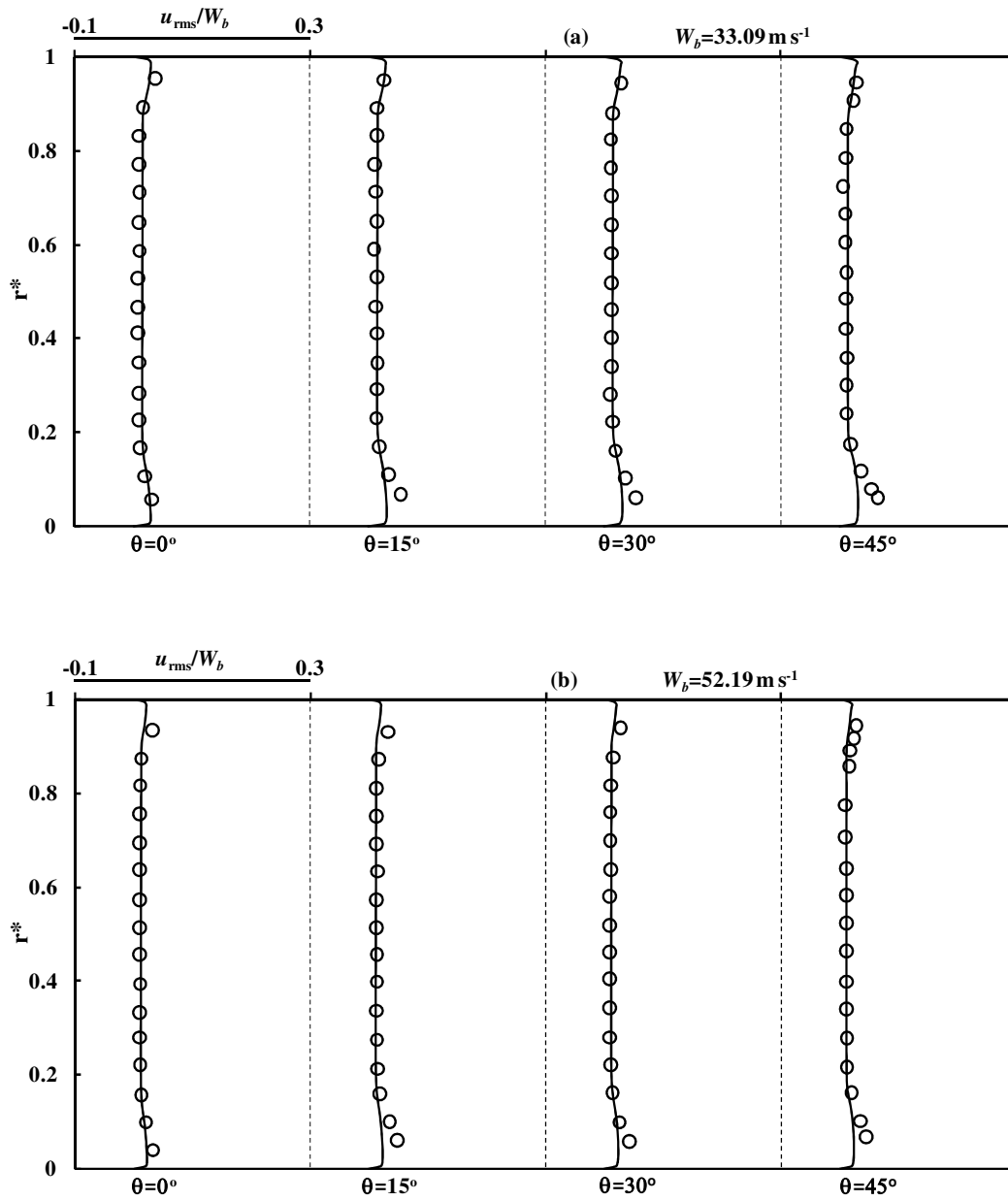


Figure 6

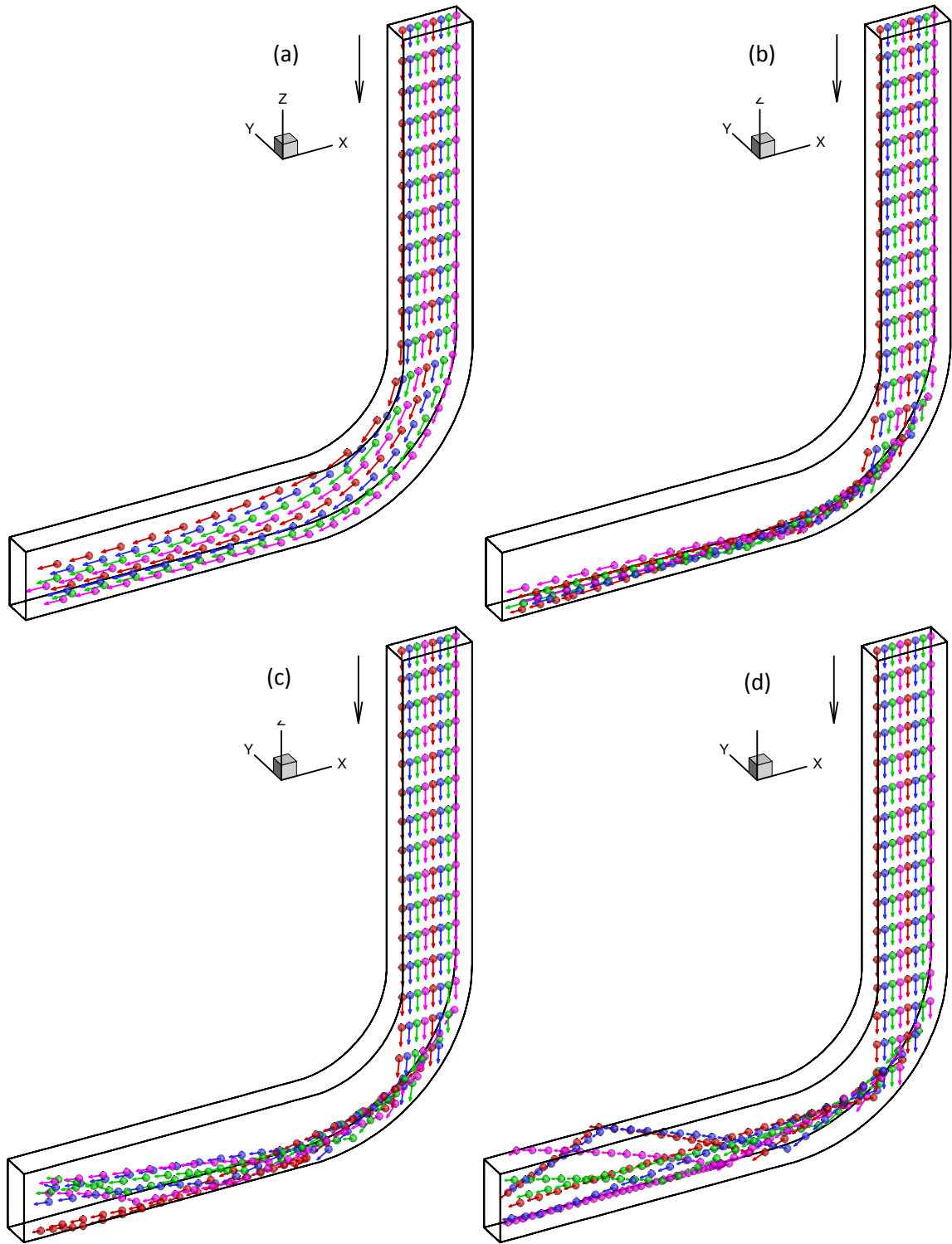


Figure 7

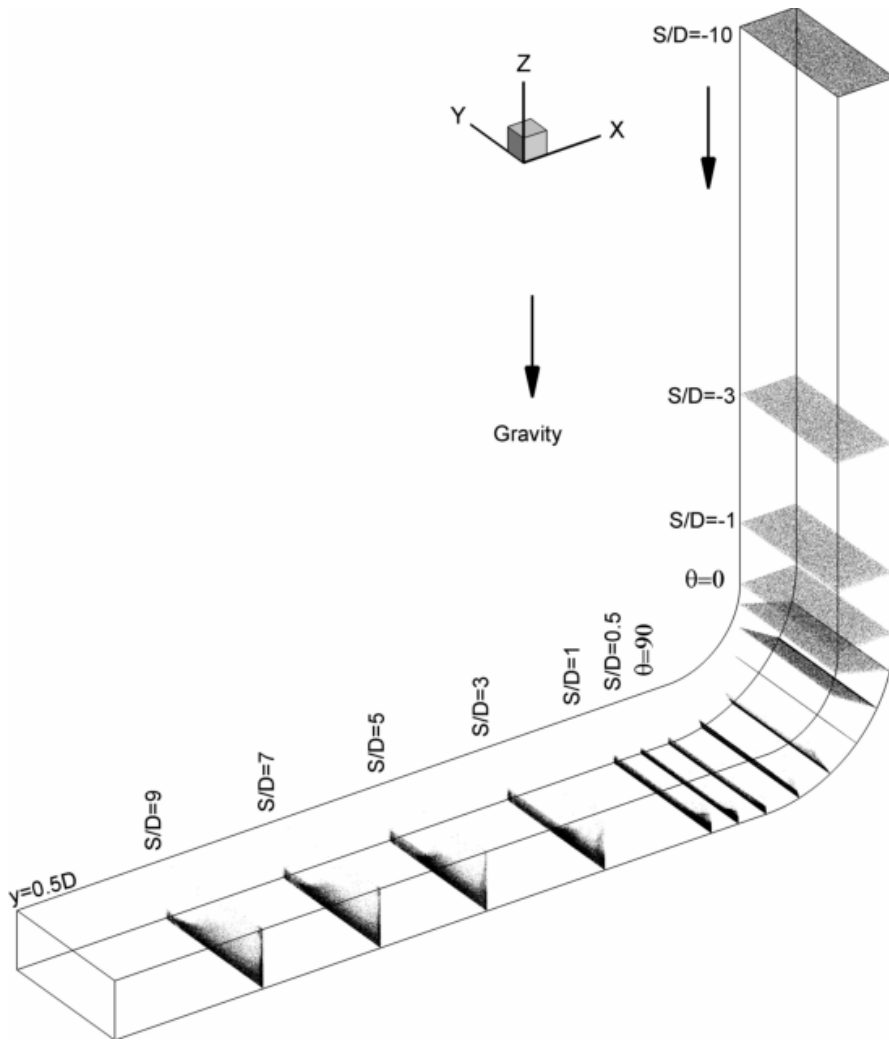


Figure 8

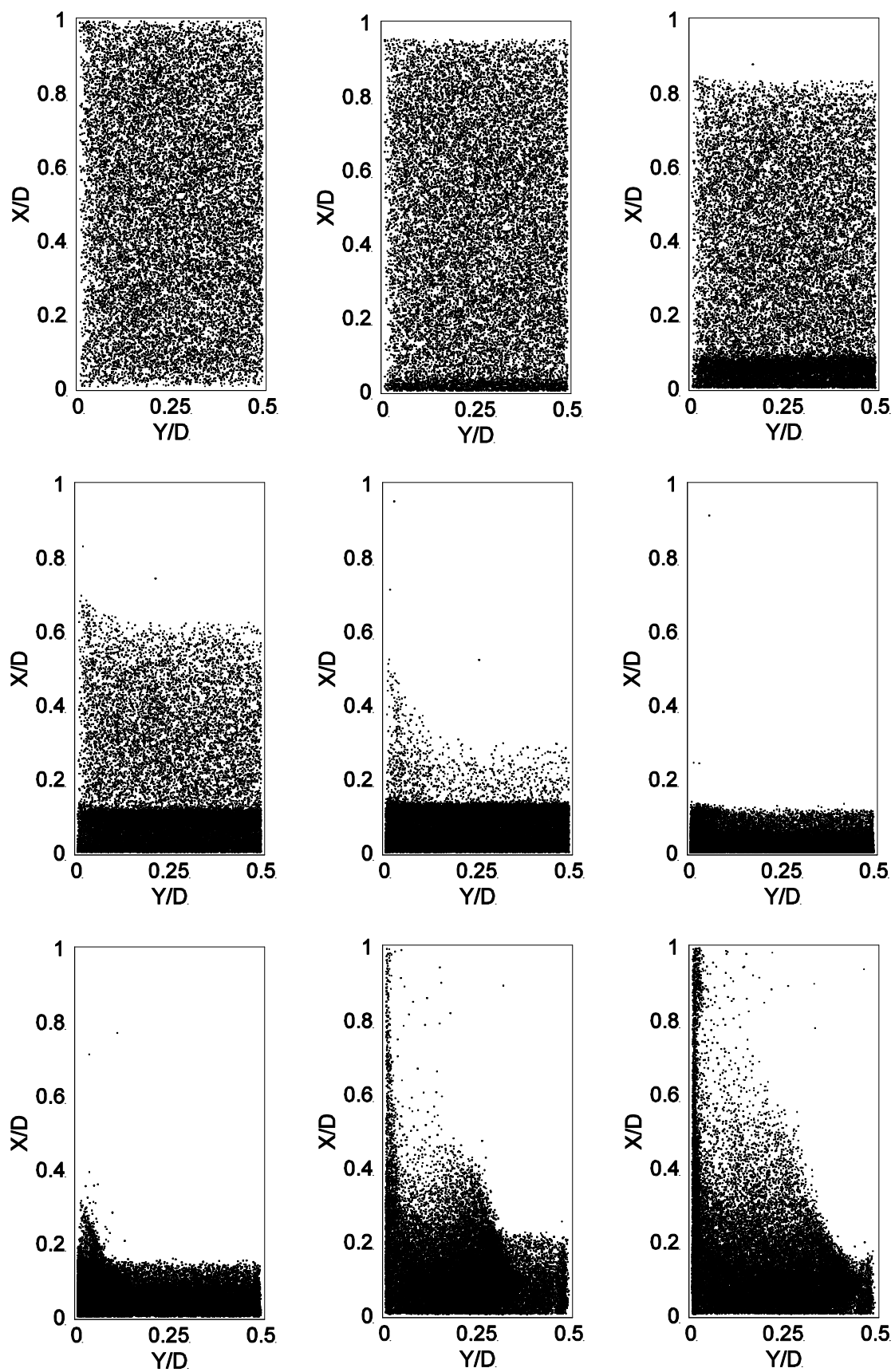


Figure 9

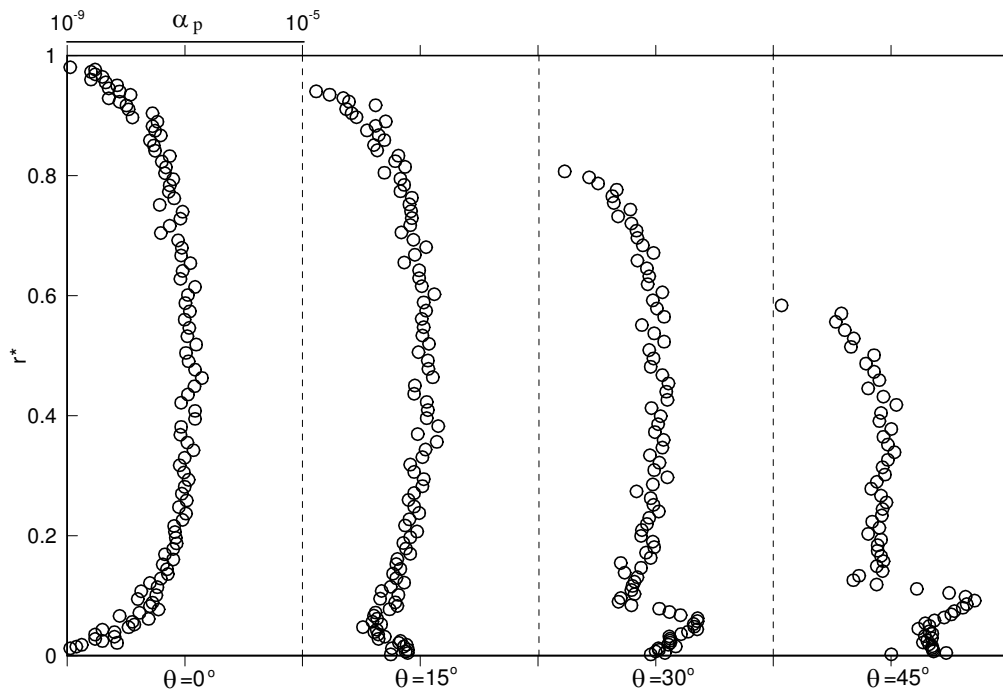


Figure 10

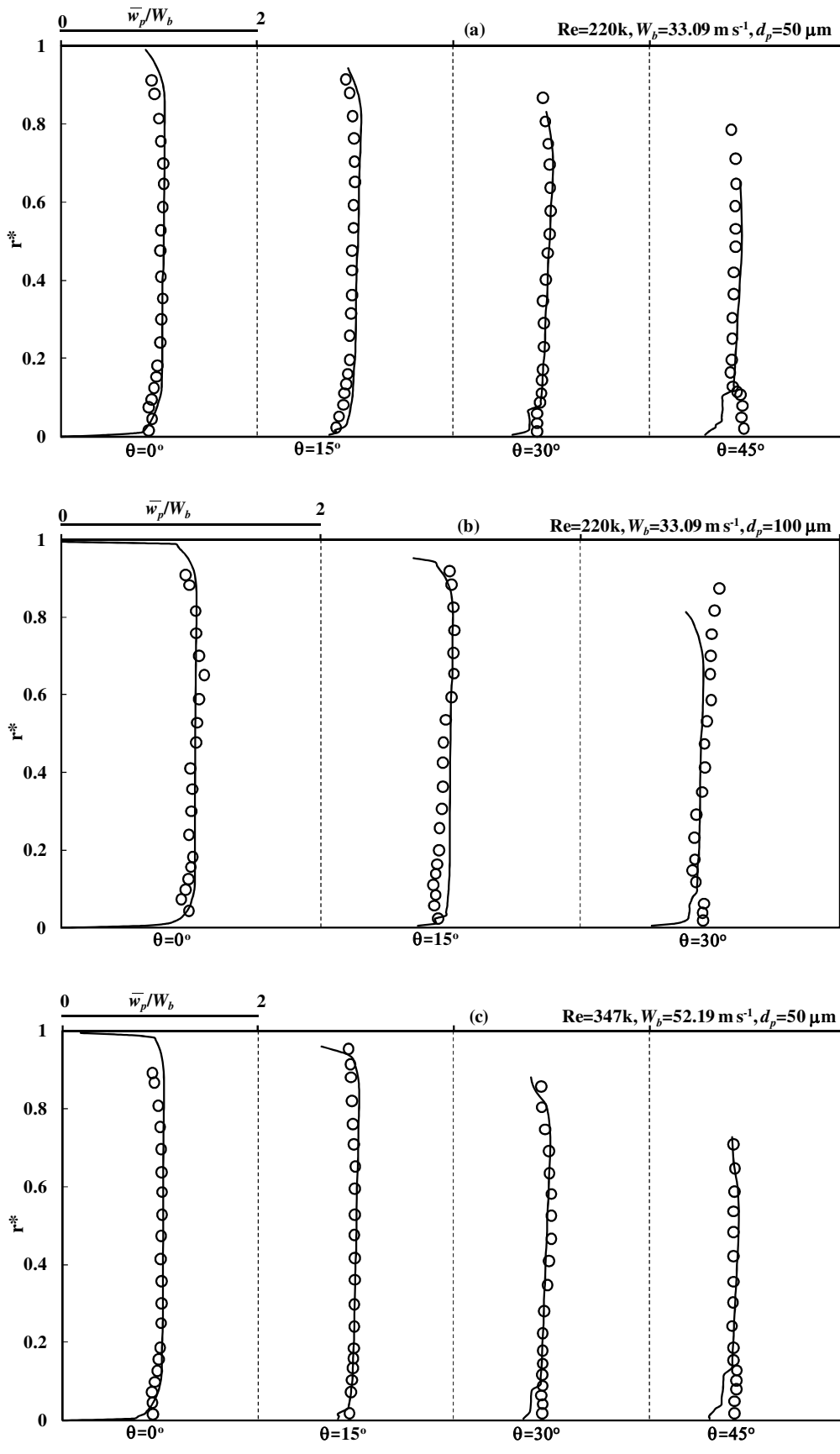


Figure 11

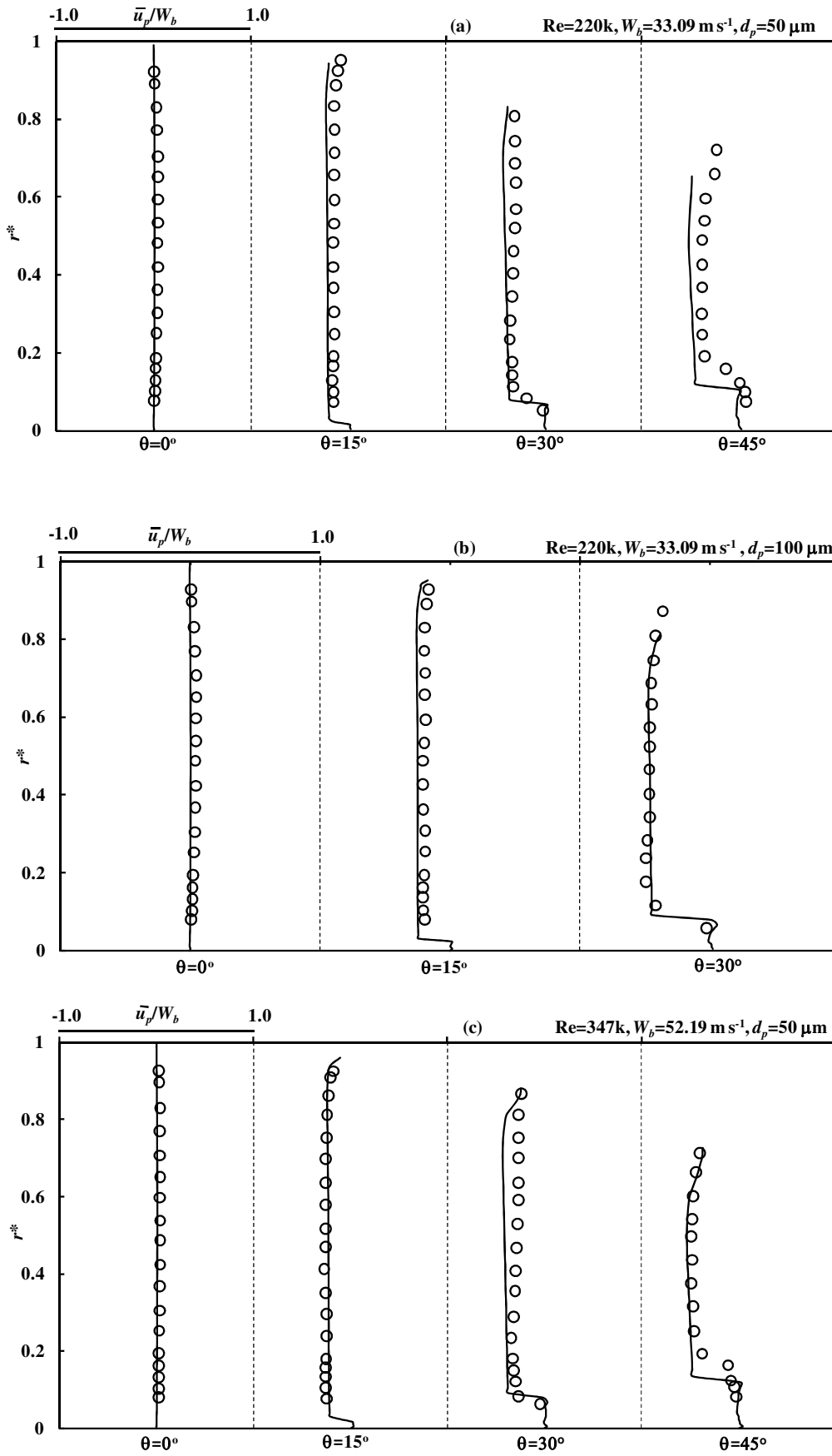


Figure 12

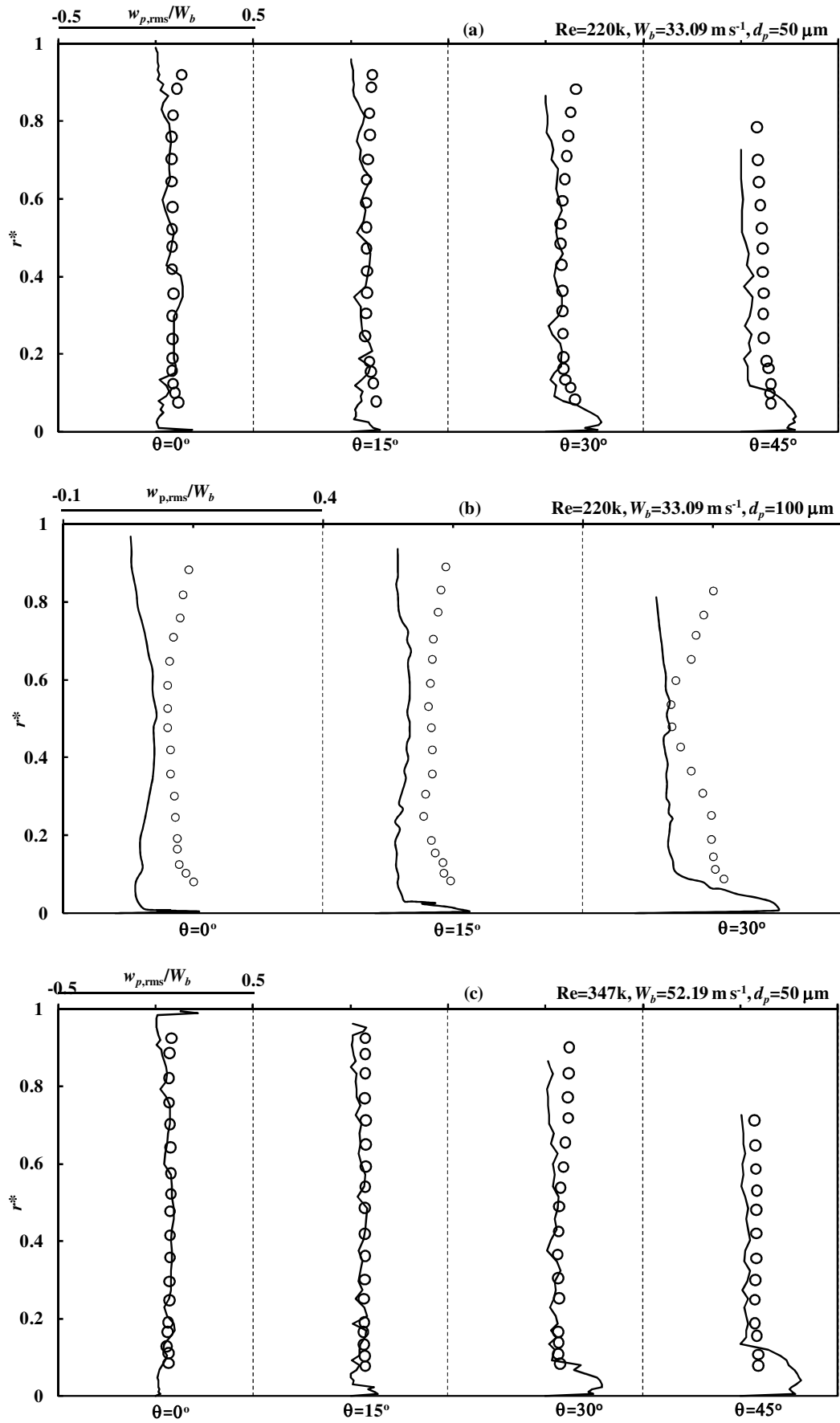


Figure 13

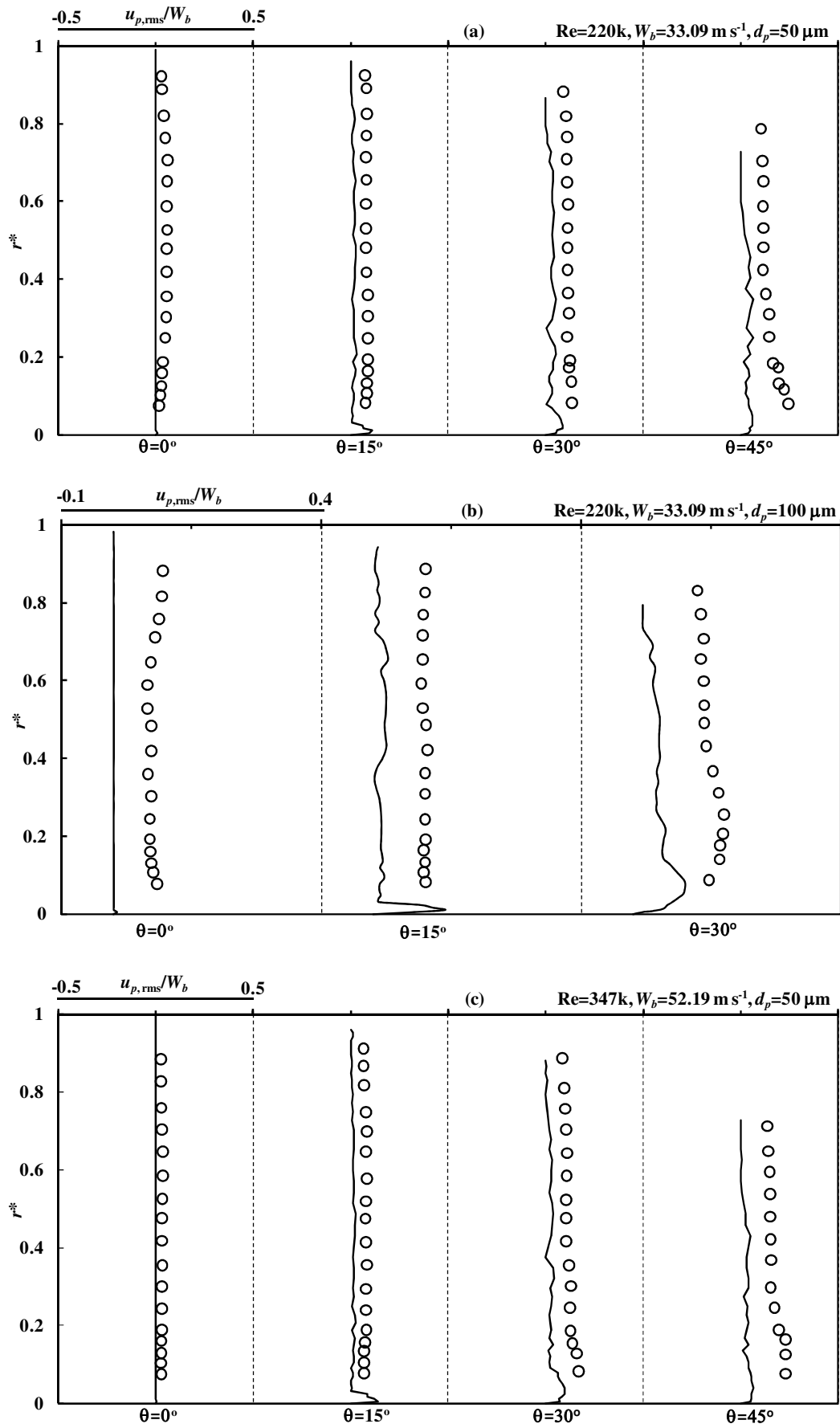


Figure 14